

# The Dynamical Evolution of the Circumstellar Gas around Low- and Intermediate-Mass stars.II. The Planetary Nebula formation.

Eva Villaver<sup>1,2</sup>, Arturo Manchado<sup>1,3</sup>, & Guillermo García-Segura<sup>4</sup>

## ABSTRACT

We have studied the effect of the mass of the central star (CS) on the gas evolution during the planetary nebula (PN) phase. We have performed numerical simulations of PN formation using CS tracks for six stellar core masses corresponding to initial masses from 1 to 5  $M_{\odot}$ . The gas structure resulting from the previous asymptotic giant branch (AGB) evolution is used as the starting configuration. The formation of multiple shells is discussed in the light of our models, and the density, velocity and  $H\alpha$  emission brightness profiles are shown for each stellar mass considered. We have computed the evolution of the different shells in terms of radius, expansion velocity, and  $H\alpha$  peak emissivity. We find that the evolution of the main shell is controlled by the ionization front rather than by the thermal pressure provided by the hot bubble during the early PN stages. This effect explains why the kinematical ages overestimate the age in young CSs. At later stages in the evolution and for low mass progenitors the kinematical ages severely underestimate the CS age. Large (up to 2.3 pc), low surface brightness shells (less than 2000 times the brightness of the main shell) are formed in all of our models (with the exception of the 5  $M_{\odot}$  model). These PN halos contain most of the ionized mass in PNe, which we find is greatly underestimated by the observations because of the low surface brightness of the halos.

*Subject headings:* hydrodynamics–ISM: structure–ISM: jets and outflows–planetary nebulae: general–stars: AGB and post-AGB–stars: winds, outflows

---

<sup>1</sup>Instituto de Astrofísica de Canarias, Vía Láctea S/N, E-38205 La Laguna, Tenerife, Spain  
[villaver@ll.iac.es](mailto:villaver@ll.iac.es), [amt@ll.iac.es](mailto:amt@ll.iac.es)

<sup>2</sup>Space Telescope Science Institute, 3700 San Martin Drive, Baltimore, MD 21218; [villaver@stsci.edu](mailto:villaver@stsci.edu)

<sup>3</sup>Consejo Superior de Investigaciones Científicas, Spain

<sup>4</sup>Instituto de Astronomía-UNAM, Apartado postal 877, Ensenada, 22800 Baja California, México  
[ggs@astrosen.unam.mx](mailto:ggs@astrosen.unam.mx)

## 1. INTRODUCTION

Low- and intermediate-mass stars experience high mass loss rates during the asymptotic giant branch (AGB) phase. Owing to the high mass loss rates during this phase, stars which have masses between 1 and  $\sim 8 M_{\odot}$  end their lives as white dwarfs with final masses below the Chandrasekhar mass limit ( $1.44 M_{\odot}$ ).

After an uncertain phase of evolution called the transition time (the timescales are not completely known), the stellar remnant<sup>5</sup> becomes hot enough to ionize the previously ejected envelope. In the meantime, the wind velocity increases and shapes the inner parts of the envelope according to the so-called interacting stellar winds (Kwok, Purton, & Fitzgerald 1978). This leads to the formation of a planetary nebula (PN). The evolution of the nebular gas from then onward depends on the energy provided by the CS through the wind and the radiation field, and both depend on the stellar luminosity and effective temperature. The post-AGB evolution of the CS is mainly determined by its core mass (Paczynski 1971; Wood & Faulkner 1986; Vassiliadis & Wood 1994 [hereafter VW94]) and by the previous AGB evolution (Blöcker 1995).

The relationship between the CS evolution and that of the nebular shells has been the subject of many observational studies (e.g., Stanghellini, Corradi, & Schwarz 1993; Frank, van der Veen, & Balick 1994; Stanghellini & Pasquali 1995; Guerrero et al. 1996; Hajian et al. 1997; Stanghellini et al. 2002). However, most of the numerical studies of PN evolution in the literature have been restricted to a  $\sim 0.6 M_{\odot}$  post-AGB evolutionary track, without allowing for the CS mass range. This lack of consideration for the CS mass range is not the only problem with the existing numerical models of PN formation. Classically, the complex AGB evolution has been modeled by a simple  $r^{-2}$  density law (Okorov et al. 1985; Schmidt-Voigt & Köppen 1987; Frank, Balick, & Riley 1990; Marten & Schönberner 1991; Mellema 1994). In the series of related papers of Schönberner et al. (1997), Perinotto et al. (1998), and Corradi et al. (2000), the previous AGB history is included; however, the grids were truncated to  $\sim 0.65$  pc, and hence only the recent mass loss history can be completely followed up. Thus, the consequences of the long term thermal-pulse AGB evolution on PN structure at large scales still need to be tested.

Our aim in this paper is to study the role that the stellar evolution and the stellar progenitor mass play on PN formation. In a previous paper (Villaver, García-Segura, & Manchado 2002 [hereafter, Paper I]) we described the dynamical evolution of the stellar wind during the AGB for low- and intermediate-mass stars. In this paper we use the gas

---

<sup>5</sup>Central star (CS) from now onwards.

structure resulting from the previous AGB evolution as the starting configuration. The PN formation is then followed by using post-AGB tracks that comprise the mass range of 0.57 to  $0.9 M_{\odot}$ , which correspond to main sequence masses of between 1 and  $5 M_{\odot}$  (Vassiliadis & Wood 1993). In §2 we describe the numerical method. The results of our models for different PN progenitors and grid sizes are presented in Section 3. In §4 we describe the observational properties derived from our models and we compare them with observations. Our conclusions are summarized in Section 5.

## 2. NUMERICAL METHOD AND COMPUTATIONAL DETAILS

The numerical simulations were done with the multi-purpose fluid solver ZEUS-3D (version 3.4), developed by M. L. Norman and the Laboratory for Computational Astrophysics. This is a finite-difference, Eulerian, fully explicit code with a modular structure that allows to solve a wide range of astrophysical problems (for further details of the numerical method see Stone & Norman 1992a,b; Stone, Mihalas, & Norman 1992).

By choosing two symmetry axis we perform 1D simulations in spherical coordinates. We use two grid sizes for each progenitor mass considered; a small one to study the development of structures in the inner parts of the nebula (between 0.5 and 1 pc), and a large one (out to 3 pc) to study the large-scale structures arising as a consequence of the mass loss during the AGB phase. All the models have a resolution of 1000 zones in the radial coordinate.

The wind evolution is implemented by setting the velocity, mass loss rate, and wind temperature in the five innermost zones of the grid. A free-streaming boundary condition was set in the outer portion of the grid. As the CS evolves, the number of ionizing photons changes, therefore we consider the evolution of the radiation field from the star together with the evolution of the stellar wind.

Photoionization has important effects on the dynamical evolution of the nebular gas. It increases the temperature and the number of particles in the gas, and thus the pressure of the photoionized gas is initially a factor of two hundred larger than the pressure of the surrounding neutral material. The dynamical effects of this increase in pressure are not negligible and must be taken into account. Since ZEUS-3D does not include radiation transfer, we use the approximation implemented by García-Segura & Franco (1996) to derive the location of the ionization front (IF) for arbitrary density distributions (Bodenheimer, Tenorio-Tagle, & Yorke 1979; Franco, Tenorio-Tagle, & Bodenheimer 1989, 1990). The position of the IF can be determined by assuming that ionization equilibrium holds at all times, and that the ionization is complete within the ionized sphere and zero outside. This implies that we are

adopting the classical definition of the Strömgren sphere, where the position of the IF is given by  $\int n^2(r)r^2dr \approx Q_o/4\pi\alpha_B$ , where  $n(r)$  is the radial density distribution,  $Q_o$  is the number of ionizing photons, and  $\alpha_B$  is the recombination coefficient to all excited levels. We apply this formulation by assuming that the nebula is pure hydrogen, that it is optically thick in the Lyman continuum, and that the ‘on the spot’ approximation is valid. However, we use solar composition for the radiative cooling which is made according to the cooling curves of Raymond & Smith (1977), and Dalgarno & McCray (1972) for gas temperatures above  $10^4$  K and according to MacDonald & Bailey (1981) for temperatures between  $10^2$  and  $10^4$  K. The unperturbed gas is treated adiabatically. Finally, the photoionized gas is always kept at  $10^4$  K, so no cooling curve is applied inside the photoionized region unless there is a shock.

## 2.1. Initial Conditions

We have set the zero-age for PN formation to be the time at which the star’s effective temperature is 10 000 K. The initial condition for each of our models is the gas structure from the previous AGB evolution (see Paper I). In this paper we assume that the transition time (the time elapsed between AGB quenching and the CS temperature reaching 10 000 K) is zero. Stanghellini & Renzini (2000) obtain zero transition times when the stellar remnant evolves on a thermal timescale.

We have studied the evolution during the PN stage for six masses whose CSs are modeled according to evolutionary tracks, taken from VW94, corresponding to stellar cores with initial masses of 1, 1.5, 2, 2.5, 3.5, and 5  $M_\odot$ . In Figure 1 we show the density and velocity structure of the gas used as the starting configuration for each model. In this plot we show the gas structure at the end of the AGB when the evolution of the stellar wind during the thermal-pulsing AGB phase is considered and the ISM density is  $1 \text{ cm}^{-3}$  (see Paper I for further details).

## 2.2. Inner Boundary Conditions: CS Evolution

The evolution of the stellar wind is computed by using the post-AGB evolutionary sequences given by VW94 for hydrogen burners with solar metallicity. This means that the stars leave the AGB while burning hydrogen in a shell. The initial and core masses of the models are given in columns 1 and 2 of Table 1.

The mechanism that drives the winds of CSs (with velocities several orders of magnitude

higher than that experienced during the AGB phase) is the transfer of photon momentum to the gas through absorption by strong resonance lines (Pauldrach et al. 1988). The dependence of mass loss rate and velocity with the luminosity ( $L$ ) and effective temperature of the star ( $T_{\text{eff}}$ ) has been adopted from VW94.

In order to find the dependence of the terminal wind velocity ( $v_{\infty}$ ; the velocity of the wind far away from the CS) on  $L$  and  $T_{\text{eff}}$ , VW94 fit a relation between  $v_{\infty}/v_{\text{esc}}$  and  $T_{\text{eff}}$  using data compiled by Pauldrach et al. (1988) for CSs of PNe. Using  $v_{\text{esc}} = \sqrt{2GM/R}$  as the stellar surface escape velocity and Stefan’s law,  $v_{\infty}$  can be written in the form,  $v_{\infty} = \beta M^{\frac{1}{2}} L^{-\frac{1}{4}} T_{\text{eff}}^{1.52}$ , where  $\beta = 16 \times 10^{-8} G^2 \pi \sigma$ .

The mass loss during the PN regime was obtained by VW94 by fitting the theoretical results of Pauldrach et al. (1988) to determine the slope of the relation between  $\log \dot{M}/\dot{M}_{\text{lim}}$  and  $T_{\text{eff}}$  which combined with  $\dot{M}_{\text{lim}} = L/cv_{\infty}$  (the maximum mass loss rate obtained by assuming that all the momentum of the stellar radiation field is injected into the wind), and with the relation obtained for the terminal wind velocity, gives:  $\dot{M} = \alpha M^{\frac{-1}{2}} L^{\frac{5}{4}} T_{\text{eff}}^{-0.85}$ , where  $\alpha = 16\pi \times 10^{11.92} \times c^{-1} G^2 \sigma$ .

In Figure 2 we show the temporal dependence of the mass loss rate and wind velocity used for our models. Note that for higher masses, the CS evolution is faster, the wind velocities are higher, and the mass loss rates are lower (different timescales are used in these plots for low- and intermediate-mass progenitors). The normalized wind kinetic energy and momentum injection rates of the wind as a function of time are shown in Figure 3. Note that the shorter timescales of the evolution are for the higher main sequence mass. The normalization factors for the wind momentum and kinetic energy are given in columns 3 and 4 of Table 1.

### 2.2.1. Ionizing Radiation from the Star

The number of ionizing photons for hydrogen,  $Q_o$ , is computed in terms of the position of the star in the Hertzsprung–Russell (HR) diagram assuming the star radiates as a blackbody. The hydrogen ionization radiation is shown in Figure 4 for the first 10 000 yr of the CS evolution. The rapid decrease in the number of ionizing photons in Figure 4 for stars with initial masses  $\leq 2 M_{\odot}$  is caused by the sudden fall in the stellar luminosity when the stellar models run out of nuclear fuel. This occurs earlier for higher mass stars since the higher the mass, the faster the evolution of the CS in the HR diagram is.

### 3. RESULTS

#### 3.1. PN evolution on Small Scales

In order to allow a direct comparison of our models with observations we have computed the  $H\alpha$  emission brightness profiles (EBPs). The emission coefficient in the  $H\alpha$  line for a nebula with a temperature of 10 000 K has the form (Osterbrock 1989)  $4\pi j_{H\alpha} = 3.5 \times 10^{-25} \cdot N_e \cdot N_p$  in  $\text{erg}^{-1} \text{cm}^{-2} \text{s}^{-1}$ . The intensity emitted by each element of volume ( $I_{H\alpha} = 4\pi j_{H\alpha}$ ) in the  $H\alpha$  line is integrated for each position in the nebula along the line of sight to derive the EBPs.

In the following, we use the brightness profile to distinguish between detached halos and attached shells. As defined in Stanghellini & Pasquali (1995), detached halos have round, detached limb-brightened outer shells, while the brightness profile of attached shell shows a change in slope rather than a dip between the shells. The brightness radial dependence for the detached halos has a form between  $r^{-2.4}$  and  $r^{-5.0}$ , while for the attached shells it is almost linear (Guerrero, Villaver, & Manchado 1998).

The results of our simulations are shown in Figures 5–10. The evolution of the density, velocity and the normalized  $H\alpha$  brightness radial distributions are shown for each mass at times which are representative of the gas evolution. These models were computed at radial scales that allow us a high resolution study of the processes taking place in the inner parts of the nebula. The position of the IF is marked in the density profiles as a dotted line and the times at which the plots has been selected are indicated in the EBP panels. Note that both the time at which the plots have been selected and the time interval between them are different for each stellar mass.

As the CS evolves, the wind velocity increases reaching a velocity above which the shocked gas is not able to cool down radiatively. An adiabatic shock then develops at the interaction region between the high velocity stellar wind and the dense material ejected previously during the AGB. The thermal energy provided by the hot bubble formed by this adiabatic shock will subsequently compress the gas in the innermost regions, forming a shell. In our models during the early phases of the evolution, either the hot bubble is not formed, or it cannot compete with the increase in pressure caused by the photoionization.

In Figure 5 we show the evolution of the gas for the  $1 M_{\odot}$  model. Owing to the highly supersonic expansion velocity of the ionized region with respect to the surrounding neutral material, a shock front is formed just ahead of the IF. A thin shell can be seen in the density profiles (see the first three left panels of Fig. 5) formed by the compression associated with the shock caused by the IF. Once the innermost denser regions have been

ionized, the propagation of the IF is very fast. The propagation velocity of the Strömgren radius depends mainly on the ionization flux it receives from the star and on the density of the neutral gas. The density of the neutral material decreases with radius outside the innermost high density region, and in the early stages of the CS evolution the number of ionizing photons increases with time (see Fig. 4). The pressure gradients generated by the IF act whenever there exists a relative increase in density. Thus, the ionized gas will expand until it reaches pressure balance with its surroundings, and so it can be seen how the gas behind the IF expands towards the position of the CS (see the first three panels of Fig. 5 and note the negative gas velocities inward of the position of the density maximum). At this time, the hot bubble either is not yet formed or cannot provide enough pressure to stall the inwards expansion. However, as the star evolves towards higher effective temperatures, the wind velocity increases and the hot bubble is formed.

At  $\sim 4500$  yr the hot bubble is already shaping the innermost layer of the gas (the compression associated with the hot bubble makes the density of this innermost shell comparable to the one caused by the IF). At this time the EBP shows a double-peak in the innermost parts of the nebula. The innermost peak is caused by the hot bubble; the outermost peak is the consequence of an inward shock wave caused by the photoionized gas. The latter moves towards the position of the CS, and as the contact discontinuity advances, the two shells merge. At this time all the gas is ionized and two attached shells that surround the innermost double peak structure are also visible, one at  $\sim 0.1$  pc and a fainter one at  $\sim 0.15$  pc. These attached shells are not the consequence of the passage of the IF, rather they are formed by the expansion of the H II region in a stratified medium. The intermediate attached shell eventually becomes a detached shell with approximately 11% of the brightness of the main inner shell and its expansion velocity is  $\sim 22$  km s $^{-1}$  (see the bottom panel in Fig. 5).

In Figure 6 we show the evolution of the  $1.5 M_{\odot}$  model. In this case we can see that, as in the  $1 M_{\odot}$  case the shell formed by the propagation of the IF is the brightest one during the first 3000 yr of evolution. At 5500 yr this shell has become detached and surrounds the shell formed in the innermost regions by the hot bubble. This detached shell is still visible in the EBP panels at 8000 yr and propagates outwards with a velocity of about 30 km s $^{-1}$ .

The evolution of the  $2 M_{\odot}$  model is shown in Figure 7. The gas evolution and the kinds of shells that are formed are very similar to those formed for the  $1.5 M_{\odot}$  case, in spite of the difference in timescales, energy input, and initial gas density conditions. The shell formed by the IF is again the brightest one during the early stages of the evolution ( $\sim 3000$  yr) and it evolves into a detached shell when the shell formed by the hot bubble appears in the innermost regions of the gas.

The models with initial masses of 2.5, 3.5, and  $5 M_{\odot}$  spend a very short time on the

horizontal, constant luminosity part of the HR diagram. Moreover, the injection of kinetic energy reaches its maximum value earlier for higher mass progenitors (see Figs 2 and 3). In Figure 8 we present the evolution of the  $2.5 M_{\odot}$  model and we can see that it is not yet fully ionized after 5500 yr, so that only one shell appears in the EBPs. This single shell is associated with the propagation of the IF, since the compression associated with the wind–wind interaction process has not yet started.

The evolution for the  $3.5 M_{\odot}$  model is shown in Figure 9. Two shells appear in the nebular structure when all the gas is ionized; a bright main shell and surrounding it an attached shell. The dynamical evolution of the brightest main shell is controlled by the kinetic energy provided by the wind since the very early stages of the evolution. Note that at about 1000 yr the wind kinetic energy has already reached its maximum value (see Fig. 3), and that, therefore, the hot bubble is already efficiently compressing the innermost layers of the gas.

Only one shell is formed in the model with  $5 M_{\odot}$  (shown in Fig. 10) which is associated with the IF. The luminosity drop at the turn-around point for this model  $\sim 150$  yr after the star has reached a temperature of 10000 K. Note in Figs 3 and 4 the rapid decrease in the number of ionizing photons, wind momentum and energy for this model. The EBPs are uniform with an enhancement at the edge. This is the only model that does not produce a multiple shell structure and the only one that results is an ionization-bounded PN.

Our models may be overestimating the pressure in the boundary between neutral and ionized gas because of the approximation we used for the photoionization. First, near the Strömgren radius the ionization degree decreases sharply over a distance which is proportional to the mean free path of a photon in the neutral gas. However, because of the mean free path photon dependency with density, as the density decreases the mean free path increases and the edge between ionized and neutral material begins to have a non-negligible thickness with respect to the size of the Strömgren radius. We have used the classical Strömgren sphere approximation for the photoionization; therefore, the boundary between the ionized and neutral material is a discontinuity in our models that could lead to an overestimate in the pressure at the IF when the density of the medium is very low. None the less, in our simulations the IF is never trapped in the low density media and we do not expect our gas velocities to be overestimated owing to this effect. Second, we assumed that ionization equilibrium holds all the time, and that ionization is complete inside the Strömgren radius. If the IF moves slowly (in case of very high density media or low ionizing photon flux), recombination occurs within the ionized volume. The presence of neutral atoms inside the Strömgren volume reduces the number of photons arriving at the IF, which therefore slows down or even stalls. This might affect our  $2.5$  and  $5 M_{\odot}$  models since these are the only



ones for which the IF is trapped in the high density media for a long enough time for recombination to take place. A full consideration of radiation transfer will not change our main results (for details of how radiation transfer shapes PNe the reader is referred to Mellema 1994; Osterbrock 1989; Corradi et al. 2000).

We can only compare the  $2.5 M_{\odot}$  model computed on small scales since this is the only model with a PN track close enough to the  $0.6 M_{\odot}$  track considered in previous numerical models available in the literature. We find good agreement with the kinds of structures formed in the models of Mellema (1994, performed at 0.25 pc) or Corradi et al. (2000, performed at 0.65 pc) on intermediate scales, despite the differences in the departure conditions, stellar evolutionary models, and radiation transfer approach. Intermediate detached and attached shells are also formed in those models.

### 3.2. PN Evolution on Large Scales

We have shown in Paper I that large-scale structures appear in the circumstellar gas when the evolution during the AGB phase is considered. The shells formed during the AGB phase have not diluted by the time the PN phase starts (see Fig. 1). With the aim of studying these outer shells during the PN phase we performed numerical simulations using grid sizes that ensure that we do not lose matter at the outer boundary. Here we present these models performed on larger radial scales as radial distributions of density, velocity, and  $H\alpha$  EBP diagrams in Figs 11, 12, 13, 14, 15, and 16 for the range of initial-mass models considered previously. In order to show on the same graph the normalized emission of the brightest shell and the faint emission of the outer shell, we have plotted the EBPs at two intensity scales.

The model with  $1 M_{\odot}$  is shown in Figure 11. At 4000 yr an outer detached shell with a radius of  $\sim 1.3$  pc and 5000 times fainter than the brightest inner shell<sup>6</sup> is present. The outer shell is formed as a consequence of the density structure generated by the previous AGB evolution. It is not a signature of a thermal pulse and is formed owing to a shock in the interaction region between two consecutive enhancements of the mass loss rate during the AGB (see Paper I). A similar detached shell is present in the other models (Figs 12, 13, 14, and 15), but in the one with  $5 M_{\odot}$  (Fig. 16). The radius of the outer shell in the 1.5, 2, 2.5, and  $3.5 M_{\odot}$  models is  $\sim 2$  pc. The ratio between the emission of the main shell and that of the outer shell decreases as the intensity of the main shell decreases during the evolution (the analysis for the different masses is discussed in § 4.2.3). This brightness ratio does not

---

<sup>6</sup>We will refer to this shell as the main shell from now onwards.

decrease steadily because the formation of the hot bubble causes a sudden increase in the main shell brightness. The evolution of these low brightness outer shells is only affected by the ionization of the gas in the time the PN evolves, which is short compared to the evolution during the AGB phase. The fast wind is not relevant in their evolution since it only affects the innermost regions of the gas structure. The photoionization generates pressure gradients which broaden the outer shells and smooth out the density structure on large temporal scales. The  $H\alpha$  emission brightness of the outer shells decreases with radius and shows a limb brightened edge. Therefore these shells can be interpreted as detached halos. On the radial scales shown intermediate detached and attached shells are also present although they are difficult to see.

In the  $5 M_{\odot}$  model, the outer regions are not ionized and therefore only a single shell is formed. A neutral dense shell is also present (see the density profile in Fig. 16) at  $\sim 2$  pc. Although this neutral shell contains a huge amount of material, we do not expect it to be detectable in  $H_2$ , as it is very far away from both the CS and the photodissociation region for any excitation mechanism in  $H_2$  emission to be efficient.

### 3.3. The Different Shell Formation Processes

#### 3.3.1. The Main Shell

In a PN, the inner shell is the main observable feature because of its brightness, so it is the most widely studied region. The properties of the main shell change from nebula to nebula, independently of morphology. Since the energetic input of the CS directly determines the evolution of this shell, it is very likely that its radius and expansion velocity are directly related to the evolutionary status of the nebula and to the mass of the stellar progenitor.

According to our models the main observable feature of the PN during its early evolution is that associated with the propagation of the IF. The total time that this shell is the main observable feature depends on the progenitor mass, and is  $\sim 3000$  yr for the models with masses of 1, 1.5, and  $2 M_{\odot}$ , more than 5000 yr for the model with  $2.5 M_{\odot}$ ,  $\sim 1000$  yr for the  $3.5 M_{\odot}$  model, and during the whole evolution for the  $5 M_{\odot}$  model. We find excellent agreement with the analytical predictions of Breitschwerdt & Kahn (1990), who found that during the first 2000–3000 yr of evolution the ionized region is the dominant feature of the PN. Afterwards, the evolution of the main shell depends on the kinetic energy provided by the hot bubble. The temporal evolution of the radius and expansion velocity of the main shell is discussed in Section 4.1.

### 3.3.2. *The Intermediate Attached and Detached Shells*

With the exception of the  $5 M_{\odot}$  model, attached and detached intermediate shells, that surround the main innermost shell, are formed for all the models. Detached and attached intermediate shells have different formation processes. The detached intermediate shells are formed by the effect of the propagation of the IF. The main shell is that formed by the IF until the hot bubble develops. When the hot bubble develops a shell brighter and closer to the CS is formed (becoming the main shell) and the shell that was formed by the IF becomes secondary in brightness with a EBP that decreases more steeply than  $r^{-2}$  and show a limb-brightened edge, i.e., a detached intermediate shell.

The attached shells, which are characterized by a linear decrease in EBP, are a consequence of the previous radial density structure. In contrast to what has been suggested previously (Mellema 1994; Schönberner et al. 1997), we find that the attached shells are not necessarily formed by the dynamical effects of the photoionization of the gas, since they still appear in the artificially computed EBP of test models in which the photoionization was switched off.

The attached intermediate shells show almost constant velocities around  $20 \text{ km s}^{-1}$ , and the detached shells, since they have been accelerated by the IF, have velocities up to  $10 \text{ km s}^{-1}$  larger than those of the attached shells. With time, the detached intermediate shells may not be discerned from the attached shell. Guerrero et al. (1998) determined the expansion velocities of a sample of PNe that present multiple shells. They found that the average expansion velocity of the attached shells in their sample was  $25 \text{ km s}^{-1}$ , which is in agreement with our results.

### 3.3.3. *The Detached Halos*

The models computed at larger radial scales show that a faint shell surrounding the main and the intermediate attached and detached shells is present. We refer to these shells as outer detached shells or halos. The imprint of the wind history experienced by the star is mainly present in this outer detached shell. Although the emission arising from the outer parts is faint compared to the emission from the main shell, deep optical CCD images should reveal the existence of the outer shells, as long as these are ionized.

The outermost detached shell is a consequence of the previous density structure, i.e., the shell formed during the AGB phase, and its size is mainly controlled by stellar evolution, although the ISM pressure also plays a role (see Paper I, where we showed how the signatures of the modulations in mass loss consequence of the thermal pulses during the AGB are not

recorded in the gas structure). The shells formed by shocks in the interaction regions between two subsequent periods of enhanced mass loss are the only remaining stable structures. These are the shells visible during the PN stage in the form of faint external detached shells or halos (note the huge difference in brightness between the main and outer detached shell in Figs 11–15). According to our models, the dynamical times derived from observations of PN halos cannot be correlated with the theoretical timescales between thermal pulses. A detailed analysis of the evolution of brightness ratio, velocity and radius of these shells is presented in Section 4.2.

#### 4. DERIVED OBSERVABLE PROPERTIES

Comparing the results of the models with observations requires some caution. Depending on the emission line observed, different linear sizes and expansion velocities are measured. In many nebulae there is a difference in the expansion velocity measured in low ( $H\alpha$ ,  $[N\ II]$ , and  $[O\ II]$ ) and high excitation ( $He\ II$ ,  $[O\ III]$ , etc.) emission lines (this is the so-called Wilson effect [Wilson 1948]), with the low excitation lines having the largest expansion velocities. Moreover, most of the velocity determinations in PNe have only been obtained for the brightest inner regions, and all the distance-dependent parameters suffer uncertainties because of the poorly determined distances in Galactic PNe. Kinematical studies of outer shells are scarce and also have the problem that their receding and approaching velocity components are unresolved. Chu, Jacoby, & Arendt (1987) offer a complete discussion on how distance and nebular evolution hinder the detection of faint outer shells in PNe.

From our models we have derived properties that can be used to compare with the observations. Since we have assumed spherical symmetry in our models the results and the discussion hereafter exclude comparison with PNe having bipolar morphology. The detached outer shells of PNe are mainly detected in  $H\alpha$  or  $[O\ III]$ ; no emission is usually found in  $[N\ II]$ . All the analysis from now onwards is made in the  $H\alpha$  recombination line.

We should point out here that our models assume a homogeneous ISM as well as an smooth AGB gas ejection. PNe shells are far from being homogeneous and very often show different kinds of gas condensations, cometary tails, and low ionization emission regions (Balick et al. 1998). Different mechanisms may be responsible for the formation of these small scale structures in PNe; i.e. instabilities, AGB, and ISM clumps that may have important consequences on the gas dynamics (Dyson et al. 2000). Dyson et al. (1989) suggested that the clumps are formed in the envelope of the AGB star and studied the conditions needed for its survival to the PN phase. The clumpy nature of AGB winds has been widely observed in molecular lines (Olofsson et al. 2000). A clumpy AGB wind ejection alters the structure

of the shocks (cf. Williams & Dyson 2002), and if the clumps are massive enough to survive the harsh environment they will probably act as broken walls through which the flow will go (with a modified density and velocity). It is possible that the main shell formation will be influenced by the clumpy nature of the AGB wind, but not the outer shells, as it is very unlikely that a massive condensation can travel so far away from the star to directly influence the halo formation. We think that the development of instabilities in the flow is a more plausible explanation for the presence of small scale structure in the PN halos. We expect that only the external shells of the high mass progenitors ( $3.5$  and  $5 M_{\odot}$ ) may be affected by a clumpy nature of the ISM since only in these models is the halo formed by the compression associated with a shock between the AGB wind and the ISM material.

It is very likely that these mechanisms are operating all together in real PNe, and until detailed 2D numerical simulations that take into account all of this effects are performed we can only speculate on the relative importance of one or another.

#### 4.1. The Main Shell

##### 4.1.1. *The Evolution of the Radius*

We have computed the evolution of the main shell radius from the position of the maximum of the  $H\alpha$  brightness profiles (see Fig. 17). The position of the inflexion point in the curves of Fig. 17 is determined by the point where the shell produced by the impinging of the hot bubble evolves into the brightest shell. Before this point, the brightest shell is formed by the compression associated with the IF.

##### 4.1.2. *Kinematics*

In order to study the kinematical evolution of the shells in our models, we have computed the  $H\alpha$  synthetic line spectrum. The intensity,  $I(x, v)$ , measured at a given projected distance,  $x$ , for a velocity  $v$  can be computed by convolving each value of the component of the velocity vector along the line of sight,  $v_y$ , with the emissivity function,  $\epsilon(r)$ , and with the velocity distribution function  $\varphi(v, T_e, v_y)$ . The velocity and emissivity radial distributions are taken from the simulations, and we have assumed that the electron temperature has a constant value of  $10\,000$  K.

We have used a spectral resolution of  $1 \text{ km s}^{-1}$ . In the computed line intensity velocity profiles through the center of the nebula, the receding and approaching components arising

from the higher density region overwhelm the emission of the other shells. The expansion velocity of the brightest shell is calculated directly from the line intensity velocity profiles.

We have computed synthetic  $H\alpha$  spectra for the photoionized gas at each output of the simulations, and have derived the expansion velocity of the brightest shell. The temporal dependence of the main shell velocity is shown in Fig. 18 for the first 10 000 yr of the PN evolution. The temporal resolution of the curves depends on the model and is typically between 135 and 400 yr. In all cases, the data have been smoothed using a window of width twice that of the resolution element.

All the models show expansion velocities  $\sim 20 \text{ km s}^{-1}$  during the early stages when the dominant feature is the shell caused by the IF. The shell is accelerated when the density of the innermost shell, forced by the thermal pressure provided by the hot bubble, is larger than the value of the shell formed by the passage of the IF. From then onwards, this shell is driven at the expense of the thermal pressure of the hot bubble, and its velocity increases rapidly with time. As the CS evolves towards lower effective temperature, the wind kinetic energy decreases (see Fig. 3), and, moreover, the adiabatic expansion of the hot bubble decreases its thermal pressure. These two processes combined together explain why the velocity of the main shell is slowed down at later stages during the evolution.

#### 4.1.3. *Radius versus Expansion Velocity*

In our models neither the expansion velocity of the nebula nor its radius increases monotonically with age. With the aim of exploring a possible correlation between these two observables we have plotted in Fig. 19 the radius and expansion velocity of the inner shell at each time we have an output from the simulations. We show the relation for a maximum radius of 0.5 pc. The total time shown is therefore different in each of these panels as it depends on the time the model needs to reach this radius (see Fig. 17).

Since in Fig. 19 the time is the hidden variable (for each time we plotted pairs of radius and velocity of the inner shell) more than one expansion velocity may correspond to one value of the radius (i.e. for the  $1 M_{\odot}$  star). The radius of the inner shell (defined as the maximum in the emissivity) for this model increases with time at the very beginning of the evolution, then decreases (with the rarefaction wave caused by the IF) and later it is more or less constant until the moment a hot bubble is formed and takes control of the inner shell (see Fig. 17).

For the intermediate cases (2, 2.5, and  $3.5 M_{\odot}$ ), Fig. 19 mainly reflects the temporal evolution of the expansion velocity of the inner shell (see Fig. 18) because of the almost

monotonically increase of the radius of the inner shell with time for these models (see Fig. 17).

We find low velocities at small radii for all the models. For radii larger than  $\sim 0.2$  pc only the  $1.5 M_{\odot}$  model shows a monotonic increase in velocity with radius. In the 2 and  $2.5 M_{\odot}$  models, the velocity increases with radius up to  $\sim 0.25$  pc decreasing afterwards. In the  $5 M_{\odot}$  model the velocity remains almost constant around  $20 \text{ km s}^{-1}$  as the radius increases. The same behavior is shared by the  $3.5 M_{\odot}$  model but after a velocity increase with radius up to  $\sim 0.1$  pc. The evolution of the energetic input of the CS explains the behavior at larger radii. The more massive nuclei fade faster in the HR diagram, the hot bubble is depressurized by its adiabatic expansion, and the main shell velocity decreases, even though its radius is still increasing. The behavior at small radii (i.e., a young nebula) is related to the IF.

The observed main shell sizes and expansion velocities in PNe are spread over a wide range, with a tendency of the expansion velocity to increase with radius up to  $0.2$  pc (Sabbadin 1984b; Bianchi 1992) while for larger radii the scatter is very large. Our models for different masses show the same tendencies. As suggested by Sabbadin (1984a) and Weinberger (1989) in order to explain the observed scatter of the expansion velocity versus radius in PNe, we find that the behavior of the expansion velocity versus the radius depends on the evolution of the CS energetics and subsequently on the progenitor mass.

#### 4.1.4. *Kinematical versus CS Ages*

The most common way of deriving the evolutionary status of a PN is through its kinematical age (the ratio between the radius of the shell and its expansion velocity). Obtaining ages from empirical determination has two fundamental problems. First, they are subject to the distance uncertainties in determining the physical size of the nebula. Second, as we have shown previously, the nebular shells are subject to acceleration during the PN evolution.

It has been widely assumed that the kinematical ages can be compared with the evolutionary timescales of the CS. However, there is some disagreement when this comparison is made. McCarthy et al. (1990) found a strong trend for old nebulae to be located at the position of young CSs. When the sample is biased towards low mass progenitors the tendency is in the opposite sense (Gathier 1984, and some low-mass objects in the sample of McCarthy et al. 1990) and young nebulae appear to be hosted by old CSs. In order to investigate this observed disagreement between the kinematical and CS timescales, we have computed the kinematical age of the nebula derived from our models and we plot it in Fig. 20 versus the

age of the CS.

We find that the kinematical ages are always higher than the CS ages when the nebula is younger than 5000 yr, whilst for intermediate ages (between 5000 and 10 000 yr) the ages derived from a dynamical analysis tend to overestimate the age of the CS for high mass progenitors (3.5 and 5  $M_{\odot}$ ) and underestimate it for the low mass progenitors (1, 1.5, 2, and 2.5  $M_{\odot}$ ). Thereafter, the tendency is maintained except for the models with 2, 2.5, and 3.5  $M_{\odot}$ , for which the kinematical ages agree well with the CS ages.

This result can be explained by the fact that during the early stages of the evolution the main shell is a consequence of the IF. The radius is larger during early stages of the evolution than later on when the hot bubble shapes the main shell (see Figs 5 and 6). Moreover, the velocity of the shell is slower at the early times when it is determined by the IF, making the kinematical age even higher. Later on, the situation changes; when the hot bubble drives the main shell, the radius becomes smaller and the expansion velocity increases making the kinematical ages decrease (1, 1.5, 2, and 2.5  $M_{\odot}$ ). The tendency of the kinematical ages to be higher than the CS ages is maintained for the models with 3.5 and 5  $M_{\odot}$  because of the fast CS evolution for the former and the fact that the shell is always driven by the IF for the latter. The evolutionary timescales of the CS are reflected in the dynamical evolution of the shell.

With the results of our models we find a natural explanation for the disagreement between the kinematical timescales in PNe and the evolutionary status of their CSs that is able to account for the observed characteristics. For young CSs the dynamical ages tend to overestimate the CS ages for all the models. At later stages of the evolution, when the sample is biased towards low-mass progenitors, the dynamical ages underestimate the evolutionary status of the CSs. McCarthy et al. (1990) found transition times to be the most reasonable explanation for this disagreement. However, we find that the details of the evolution of the main shell for the different masses account for the difference in the observed timescales.



## 4.2. PN Halos

### 4.2.1. The Main-to-Halo Shell Brightness Ratio

The main nebula and the detached halo<sup>7</sup> evolve on different timescales. The former is subject to the strong interaction with the fast stellar wind, so it expands more rapidly and its H $\alpha$  emissivity decreases on a shorter timescale. With the purpose of exploring the evolution of the brightness ratio between the main nebula and the detached halo, we have computed the ratio between the peak of the surface brightness of each shell and show its temporal evolution in Figure 21. This ratio does not decrease continuously during the evolution because the density of the main shell reaches a peak (when pushed by the hot bubble) causing the maximum seen in the brightness ratios.

The surface brightness peak ratio between the main nebula and the detached halo of a sample of multiple-shell PNe observed by Guerrero et al. (1998) covers a wide range. There are a few apparently very evolved nebulae (IC 1295, M 2-2, NGC 6804, and PM 1-295) in which the detached halos are only 2–5 times fainter than the bright main nebulae. This ratio is much larger, more than 100 (MA 3, Vy 2-3, and M 2-40) or even 1000 (NGC 6826, NGC 6884, NGC 6891, and NGC 7662) for other PNe in the sample. The sample of Stanghellini & Pasquali (1995) also shows a wide range in brightness ratios. Only one PN in this sample (NGC 6751) has a ratio below 10 and is apparently an evolved nebula (16 300 yr), two show intermediate values slightly below 100 (M 1-46 [5,700 yr; Guerrero et al. 1996], NGC 6629 [ $\sim$ 3,000 yr], and Cn 1-5 [no CS age provided]). NGC 2867 (evolving through a helium-burning track), and Tc 1 (apparently young) have values of between 100 and 500. The detached shells in the sample of Chu et al. (1987), for which the measurements of the main to outer surface brightness peak ratios are available, are NGC 2438 ( $\geq 143$ ), NGC 6543 ( $\geq 667$ ) and NGC 6720 ( $\geq 200$ ), no evolutionary status of the CS is provided.

In our models the extremely low (less than 10) emission brightness ratios are only reached for very evolved CSs. Larger ( $\geq 500$ ) ratios are found only during the early stages of the evolution, i.e. for young CSs. It is clear that the observation of these outer external shells in PNe may be difficult because of the huge brightness contrast between the main shell and the halo.

---

<sup>7</sup>The discussion hereafter excludes the 5  $M_{\odot}$  model since it is ionization-bounded and therefore does not show a halo.

#### 4.2.2. Radius of the Halo versus its Expansion Velocity

We show in Fig. 22 the expansion velocity of the halo versus its radius for the different models. The points represent each time we have an output from the simulations. The velocities are computed from synthetic line spectra across the center of the nebula in the same way as explained in Section 4.12. In order to obtain the expansion velocities of the halos we have performed the numerical integration starting from the position of the radius of the main shell, otherwise the emission from the main shell completely dominates the spectra.

We obtain expansion velocities for the halos that range between 8 and 17 km s<sup>-1</sup> and shell radii between  $\sim 1.3$  pc and up to 2.2 pc. In our models we find that the outer shells are confined between two shocks caused by the ionization of the structures. We find that for the 1 and 1.5  $M_{\odot}$  models the gas velocity is not constant throughout the shell.

There are very few halos for which the velocities have been measured. The observed expansion velocities of the halos in the sample of Guerrero et al. (1998) range between 12 and 28 km s<sup>-1</sup>, the average expansion velocity being 21 km s<sup>-1</sup>. Other individual determinations of the expansion velocity of the detached halos have been obtained for NGC 2022 (20 km s<sup>-1</sup>) and NGC 2438 (8 km s<sup>-1</sup>) by Chu & Jacoby (1989), NGC 6720 (25 km s<sup>-1</sup>) by Guerrero, Manchado, & Chu (1997), NGC 6751 (10 km s<sup>-1</sup>) by Chu et al. (1991), NGC 6826 (13 km s<sup>-1</sup>) by Bryce, Meaburn, & Walsh (1992a), NGC 6543 (7 km s<sup>-1</sup>) by Bryce et al. (1992b), NGC 3587 (10 km s<sup>-1</sup>) by Manchado et al. (1992), and for M 1-46 (8 km s<sup>-1</sup>) by Guerrero et al. (1996).

Our models predictions cover the same velocity range. Although we do not reach the high expansion velocities reported for some of the halos in Guerrero et al. (1998), we have demonstrated in Paper I how the expansion velocity of the outer shells increases by a factor of 1.5 on average, when the star evolves in an ISM ten times less dense.

#### 4.2.3. Main-to-Halo Shell Radii Ratio

Figure 23 shows the  $R_e/R_i$  ratio, where  $R_i$  is the main shell radius and  $R_e$  is the radius of the detached halo versus the radius of the main shell during 15 000 yr from the ionization of the halo. The radius of the outer shell changes very slowly when compared with that of the main shell. Therefore the main-to-outer shell radius ratio can be used as an indication of the evolutionary status of the nebula

All the models fall in the lower mid-plane of the plot in Fig. 23, following curves that are inversely proportional to the radius of the main shell since the evolution of the radius

of the outer shell is very slow. Therefore the curves show an evolutionary sequence, i.e., a close correlation with age, that is mainly controlled by the evolution of the main shell. The curves are displaced depending on the radius of the halo; the curve for the  $1 M_{\odot}$  model is the closest to the  $y$ -axis. The curves obtained for the models with masses 1.5, 2, 2.5, and  $3.5 M_{\odot}$  are very close together and are almost indistinguishable.

If we assume that young PNe have CS ages less than 3000 yr, we obtain an main shell radius smaller than 0.15 pc (see Fig. 17) for which  $R_e/R_i$  is greater than 10 for the  $1 M_{\odot}$  model and greater than 15 for the rest of the models. This results in PNe with detached halos more than 10–15 times larger than their main shells. Obviously,  $R_e/R_i$  decreases as the age of the nebula increases (owing to the rapid increase in the main shell radius). However, it is important to note here that the detached halos are never less than twice the size of main shells. Since the  $R_e/R_i$  ratio is distance-independent, the largest source of uncertainty in the observed data comes from  $R_i$ . As defined by Kaler (1974), giant halo PNe should have  $R_e/R_i$  greater than 5. According to our models these ratios are reached only for evolved nebulae, being even larger in earlier stages.

The outer detached radius in our models is mainly determined by the AGB evolution of the star. A smaller radius for the PN halo can be obtained only if the evolution during the thermal pulsing AGB is shortened. However, it is important not to forget the possible observational bias towards the detection of giant halos. As it already pointed out by Chu et al. (1987), the interstellar reddening at low Galactic latitudes and the intrinsic faintness of PN detached halos make them very difficult to detect.

### 4.3. Ionized Masses

We have computed the ionized mass in the grid and plotted it versus time in Figure 24. The values for the ionized masses while the nebula is optically thick are too small to be appreciable in this linear plot. When the nebula becomes optically thin to the Lyman radiation from the star, the ionized mass suddenly increases, reaches a maximum value, and remains constant from there onwards.

Previous numerical models have calculated the ionized masses in PNe (Schmidt-Voigt & Köppen 1987; Marten & Schönberner 1991; Mellema 1994). In Mellema’s models the ionized mass was found to decrease after the nebula becomes optically thin. This was caused by the small grid size used, which allowed the matter to leave the grid at the outer boundary. The ionized masses he derived were as large as  $0.22 M_{\odot}$ . Schmidt-Voigt & Köppen (1987) and Marten & Schönberner (1991) found that the ionized masses increase with time or radius;

however, these results are invalidated by numerical artifacts in the code they used.

We find that, after the nebula becomes optically thin to Lyman radiation, the ionized mass remains constant with values that are different for each stellar mass considered. Our results do not suffer from the problems that previous numerical models had in deriving the ionized masses: we have used large enough grids so the matter does not escape at the outer boundary, and in our Eulerian code, the position of the inner and outer boundaries does not change with time. Moreover, we have followed the evolution of the stars from the time when substantial mass loss rates take place (the AGB).

In Fig. 25 (solid line) we have plotted the ionized mass at 9000 yr versus the initial mass of the star. The dashed line represents the amount of ionized mass contained within the main shell. It has been computed by integrating all the ionized mass up to the first emissivity minimum after the position of the brightest shell. The dashed-dotted line represent the total amount of mass lost by the star. It can be seen that the amount of ionized mass increases with the mass of the star when the nebula is density-bounded (stellar cases 1, 1.5, 2, 2.5, and  $3.5 M_{\odot}$ ). In the case of the  $5 M_{\odot}$  star the nebula remains optically thick to the hydrogen-ionizing radiation and therefore does not follow the relation of increasing ionized mass with progenitor mass.

One might have expected the constant value reached by ionized mass (see Fig. 24) to be the difference between the initial and final mass of the progenitor; however, the ionized mass is clearly higher than this value (see Fig 25). The extra mass comes from the ISM. We showed in Paper I that the stellar wind sweeps up a high fraction of ISM matter during the AGB phase. This ISM matter swept up by the wind is not at all negligible and resides mainly in the outer detached shell. The ionized mass in the detached halos is mainly determined by the mass present in these shells at the end of the AGB phase since it does not increase substantially during the short time the PN phase lasts. Moreover, the stellar wind during the PN phase does not contribute significantly to the ionized mass because it has an extremely low density.

The estimation of ionized masses in PNe can only be made for objects for which the distances are known. The ionized masses observed cover a wide range: Boffi & Stanghellini (1994), using a Galactic sample of 31 PNe, found  $0 < M_i < 0.2 M_{\odot}$ . Pottasch (1996) determined the masses for a sample of 46 nearby PNe, and, with the exception of some objects that have high masses (4.2, 2.7, 3.5, 2, and  $1.8 M_{\odot}$  for A 74, IW 2, S 216, WDHS1, and A 7 respectively) most of the objects studied have masses between 0.01 and  $0.8 M_{\odot}$ . Ionized masses have also been determined for some individual objects:  $0.072 M_{\odot}$  for M 1-46 (Guerrero et al. 1996),  $1.17 M_{\odot}$  for the halo of NGC 6543 (Manchado & Pottasch 1989), and  $0.94 M_{\odot}$  for the halo of NGC 6826 (Middlemass, Clegg, & Walsh 1989).

Most of the observed ionized masses lie between 0.1 and 0.25  $M_{\odot}$ . We find that the observed ionized masses agree with the values obtained in our simulations when only the brightest part of the nebula is considered (dotted line in Fig. 25).

It has been claimed that the wide range of observed ionized masses is due to the ionization-bounded nature of the nebula. In the light of our results we have to disagree with this. With the exception of the 5  $M_{\odot}$  star, all the models result in density-bounded PNe. We think that a more plausible explanation is that most of the ionized masses were derived from the brightest part of the nebula.

It has also been found that larger masses are derived for lower electron densities, and that the ionized masses are correlated with the nebular radius (Pottasch 1984; Boffi & Stanghellini 1994). These correlations can be understood as an effect of the evolution. If, as we propose, the observed masses are taking into account only the mass contained in the brightest shell, as this shell evolves, its radius increases, hence encompassing more mass whilst its electron density decreases because of geometrical dilution effects.

We have to conclude that, according to our models, the observations severely underestimate the ionized mass that is present in PNe since they can recover only 0.2  $M_{\odot}$  on average. Based on a very simple momentum-conserving two-wind model, Buckley & Schneider (1995) demonstrated how standard techniques severely underestimate the ionized masses in PNe. Selection effects probably hinder the observation of the large low surface brightness part of the nebula, the PN halos, where the largest fraction of ionized matter is present.

In Table 2 we have summarized the effective temperatures of the star for which the nebula becomes density-bounded. These values are approximate because they are subject to time errors of the order of  $\sim 250$  yr, which is the average temporal resolution of the outputs in our simulations. By analyzing the observed effective temperature of PN CSs determined from different methods, Kaler & Jacoby (1991) find that PNe become optically thin for temperatures in the range 40 000–50 000 K. According to this, our models provide a very early start for the optically thin phase for the 1  $M_{\odot}$  CSs. The radii at which the transition from optically thick to optically thin nebulae takes place are also included in Table 2. The average radius is 0.11 pc, which agrees very well with the radius of  $0.12 \pm 0.02$  pc obtained by Daub (1982) for the transition.

According to our simulations, as the stellar mass increases, higher effective temperatures are needed for the transition from optically thick to optically thin PNe. Moreover, the nebula remains ionization-bounded longer for higher mass progenitors.

Table 1. Model masses and wind normalization parameters

Initial mass [ $M_{\odot}$ ]	Core mass [ $M_{\odot}$ ]	Momentum [g cm s <sup>-2</sup> ]	Kinetic energy [erg s <sup>-1</sup> ]
1	0.569	$9.3 \times 10^{25}$	$2.1 \times 10^{34}$
1.5	0.597	$1.5 \times 10^{26}$	$4.3 \times 10^{34}$
2	0.633	$2.5 \times 10^{26}$	$9.1 \times 10^{34}$
2.5	0.677	$3.4 \times 10^{26}$	$1.5 \times 10^{35}$
3.5	0.754	$5.9 \times 10^{26}$	$3.6 \times 10^{35}$
5	0.9	$1.4 \times 10^{27}$	$1.6 \times 10^{36}$

Table 2. Optically thick–thin transition radii and CS temperatures

Mass [ $M_{\odot}$ ]	$T_{eff}$ [K]	$R_i$ [pc]
1	20,000	0.0912
1.5	39,000	0.0980
2	130,000	0.1029
2.5	128,000	0.1783
3.5	207,000	0.0681
5	~	~

## 5. CONCLUSIONS

We have investigated PN formation considering the gas structure resulting from the preceding AGB as the starting point for our models, and using hydrogen-burning post-AGB tracks taken from VW94 with core masses 0.569, 0.597, 0.633, 0.677, 0.754, and 0.9  $M_{\odot}$ , and solar metallicity.

As the result of our models we highlight the importance of the dynamical effects of ionization in the shell’s evolution. During the early stages of the PN evolution the main shell is formed by the IF and is not driven by the hot bubble. We find that, with the exception of the 5  $M_{\odot}$  star model, multiple ionized shells are present in all the stellar models. The emission line profiles that characterize the attached shells result from a previous density distribution present in the circumstellar gas prior to the onset of the PN phase. The halos have sizes up to 2.3 pc (more than twice the size of the main shell) and are formed during the AGB phase, with  $H\alpha$  emissivities between 10 and 5000 times fainter than the main shell. We find that intermediate detached shells are formed in our models by the IF.

We have studied the dynamical evolution of the main shell and found that for young CSs, the kinematical ages tend to overestimate the CS ages for all the masses. At later stages of evolution, the kinematical ages underestimate the evolutionary status of the CSs when the sample is biased towards low mass progenitors. The details of the evolution of the main shell for the different masses accounts for the difference in timescales between low- and intermediate-mass progenitors.

According to our models the observations severely underestimate the ionized mass present in PNe as most of the ionized mass in PNe is contained in the detached halos, which are not usually detected because of their faintness.

We thank M. L. Norman and the Laboratory for Computational Astrophysics for the use of ZEUS-3D. We also want to thank Letizia Stanghellini, Martin Guerrero, and Tariq Shahbaz for their careful reading of the manuscript and their valuable comments. The work of EV and AM is supported by Spanish grant PB97-1435-C02-01. GGS is partially supported by grants from DGAPA-UNAM (IN130698, IN117799, and IN114199) and CONACyT (32214-E).

## REFERENCES

- Bianchi, L. 1992, *A&A*, 260, 314
- Balick, B., Alexander, J., Hajian, A. R., Terzian, Y., Perinotto, M. & Patriarchi, P. 1998,

- AJ, 116,360
- Blöcker, T. 1995, A&A, 297, 727
- Bodenheimer, G., Tenorio-Tagle, G., & Yorke, H. W. 1979, ApJ, 233, 85
- Boffi, F. R. & Stanghellini, L. 1994, A&A, 284, 248
- Breitschwerdt, D. & Kahn, F. D. 1990, MNRAS, 244, 521
- Bryce, M., Meaburn, J., & Walsh, J.R. 1992, MNRAS, 259, 629
- Bryce, M., Meaburn, J., Walsh, J.R., & Clegg, R.E.S. 1992b, MNRAS, 254, 477
- Buckley, D. & Schneider, S. E. 1995, ApJ, 446, 279
- Chu, Y.-H., Jacoby, G. H., & Arendt 1987, ApJS, 64, 529.
- Chu, Y.-H. & Jacoby, G. H. 1989, in IAU Symposium 131, Planetary Nebulae, ed. S. Torres-Peimbert (Dordrecht: Kluwer), 198
- Chu, Y.-H., Manchado, A., Jacoby, G. H., & Kwitter, K. B. 1991, ApJ, 376, 150
- Corradi, R. L. M., Schönberner, D., Steffen, M., & Perinotto, M. 2000, A&A, 354, 1071
- Dalgarno, A. & McCray, R.A. 1972, ARA&A, 10, 375
- Daub, C. T. 1982, ApJ, 612, 624
- Dyson, J. E., Hartquist, T. W., Pettini, M. & Smith, L. J. 1989, MNRAS, 241, 625
- Dyson, J. E., Hartquist, T. W., Redman, M. P. & Williams, R. J. R. 2000, Ap&SS, 272, 197
- Franco, J., Tenorio-Tagle, G., & Bodenheimer, P. 1989, Rev. Mexicana Astron. Astrofis., 18, 65
- Franco, J., Tenorio-Tagle, G., & Bodenheimer, P. 1990, ApJ, 349, 126
- Frank, A., Balick, B., & Riley, J. 1990, AJ, 100, 1903
- Frank, A., van der Veen, W.E.C.J., & Balick, B. 1994, A&A, 282, 554
- García-Segura, G. & Franco, J. 1996, ApJ, 469, 171
- Gathier, R. 1984, Ph.D thesis, University of Groningen
- Guerrero, M. A., Manchado, A., Stanghellini, L., & Herrero, A. 1996, ApJ, 464, 847



- Guerrero, M. A., Manchado, A., & Chu, Y.-H. 1997, *ApJ*, 487, 328
- Guerrero, M. A., Villaver, E. & Manchado, A. 1998, *ApJ*, 507, 889
- Hajian, A.R., Frank, A., Balick, B., & Terzian, Y. 1997, *ApJ*, 447, 226.
- Kaler, J. B. 1974, *AJ*, 79, 594
- Kaler, J. B. & Jacoby, G. H. 1991, *ApJ*, 372, 215
- Kwok, S., Purton, C.R., & Fitzgerald, P.M. 1978, *ApJ*, 219, L125
- MacDonald, J. & Bailey, M. E. 1981, *MNRAS*, 197, 995
- Manchado, A. & Pottasch, S.R. 1989, *A&A*, 222,226
- Manchado, A., Guerrero, M. A., Kwitter, K. B., & Chu, Y.-H. 1992, *BAAS*, 24, 1227
- Marten, H. & Schönberner, D. 1991, *A&A*, 248, 590
- McCarthy, J. K., Mould, J. R., Mendez, R. H., Kudritzki, R. P., Husfeld, D. Herrero, A., & Groth, H.G. 1990, *ApJ*, 351, 230
- Mellema, G. 1994, *A&A*, 290, 915
- Middlemass, D., Clegg, R. E. S., & Walsh, J. R. 1989, *MNRAS*, 239, 1
- Okorov, V.A., Shustov, B.M., Tutukov, A.V., & Yorke, H.W. 1985, *A&A*142,441
- Olofsson, H., Bergman, P., Lucas, R., Eriksson, K., Gustafsson, B., & Bieging, J. H. 2000, *A&A*, 353, 583
- Osterbrock, D. E. 1989, *Astrophysics of Gaseous Nebulae and Active Galactic Nuclei* (Mill Valley: University Science Books)
- Paczyński, B. 1971, *AcA*, 21, 417, 435
- Pauldrach, A., Puls, J., Kudritzki, R. H., Méndez, R. H., & Heap, S. R. 1988, *A&A*, 207, 123
- Perinotto, M., Kifonidis, K., Schönberner, D., & Marten , H. 1998, *A&A*, 332, 1044
- Pottasch, S.R., 1984, ‘Planetary Nebulae’, Reidel Publishing Company, Dordrecht, The Netherlands
- Pottasch, S.R., 1996, *A&A*, 307, 561

- Raymond, J.C. & Smith, B.W. 1977, *ApJS*, 35, 419
- Sabbadin, F. 1984a, *MNRAS*, 210, 341
- Sabbadin, F. 1984b, *A&AS*, 58,273
- Schmidt-Voigt, M. & Köppen, J. 1987, *A&A*, 174, 211
- Schönberner, D., Steffen, M., Stahlberg, K., Kifonidis, & Blocker, T. 1997, in *Advances in Stellar Evolution*, ed. R. Wood, & A. Renzini, (Cambridge: Cambridge University Press), 146.
- Stanghellini, L., Corradi, L.R.M, & Schwarz, H.E. 1993, *A&A*, 279, 521
- Stanghellini, L. & Pasquali, A. 1995, *ApJ*, 452, 286
- Stanghellini, L. & Renzini, A. 2000, *ApJ*, 542, 308
- Stanghellini, L., Villaver, E., Manchado, A. & Guerrero, M. A. 2002, *ApJ*, in press
- Stone, J.M. & Norman, M. L. 1992a, *ApJS*, 80, 753
- Stone, J.M. & Norman, M. L. 1992b, *ApJS*, 80, 791
- Stone, J.M., Mihalas, D., & Norman, M. L. 1992, *ApJS*, 80, 819
- Vassiliadis, E. & Wood, P. 1993, *ApJ*, 413, 641
- Vassiliadis, E. & Wood, P. 1994, *ApJ*, 92, 125 (VW94)
- Villaver, E., García-Segura, G., & Manchado, A. 2002, *ApJ*, 571, 880 (Paper I)
- Weinberger, R. 1989, *A&AS*, 78, 301
- Williams, R. J. R. & Dyson, J. E. 2002, *MNRAS*, 333, 1
- Wilson, O. C. 1948, *ApJ*, 108,201
- Wood, P., R. & Faulkner, D. J. 1986, *ApJ*, 307, 659

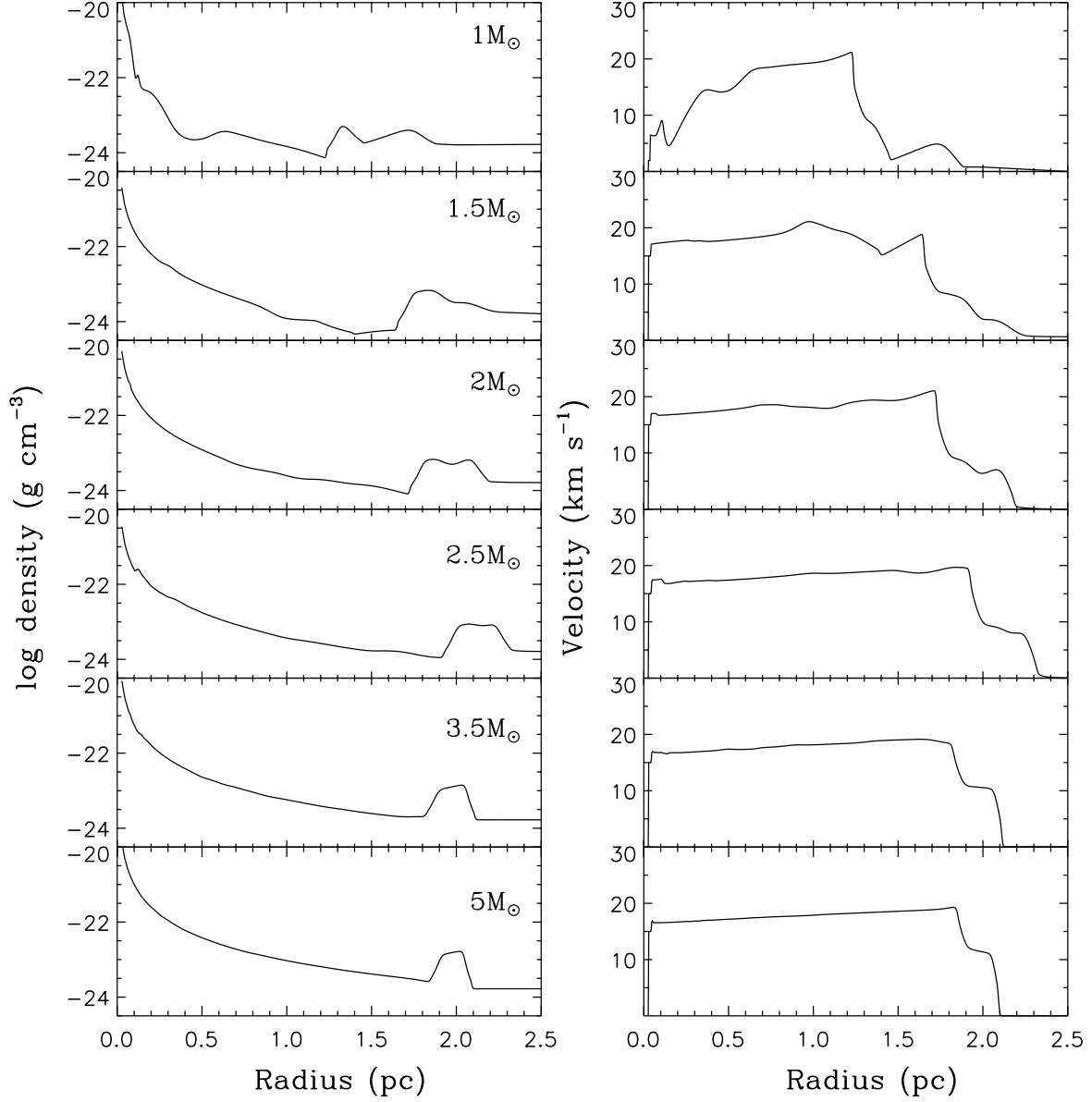


Fig. 1.— Left: logarithm of the gas density in  $\text{g cm}^{-3}$  at the end of the AGB. Right: radial distribution of the expansion velocity in  $\text{km s}^{-1}$ . From top to bottom, the initial stellar masses are 1, 1.5, 2, 2.5, 3.5 and  $5 M_{\odot}$ .

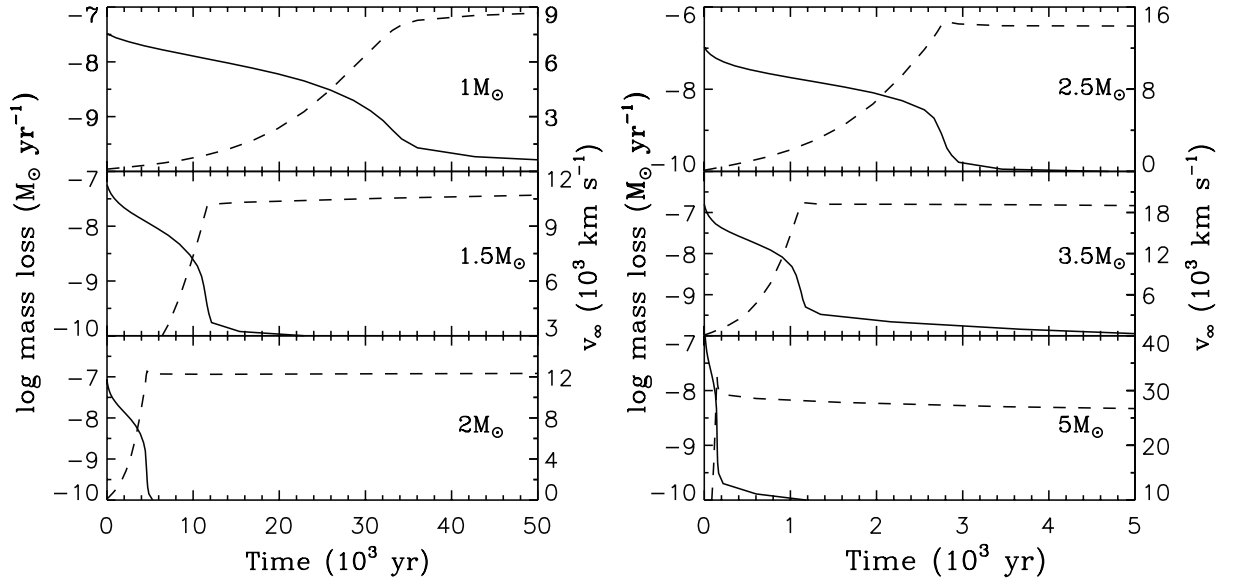


Fig. 2.— Wind parameters used for our models. Left panels: initial stellar masses 1, 1.5, and  $2 M_{\odot}$ . Right panels: initial stellar masses 2.5, 3.5, and  $5 M_{\odot}$ . The solid line represents the logarithm of the mass loss rate (left scale) and the dashed line the wind terminal velocity (right scale) in units of  $10^3 \text{ km s}^{-1}$ .

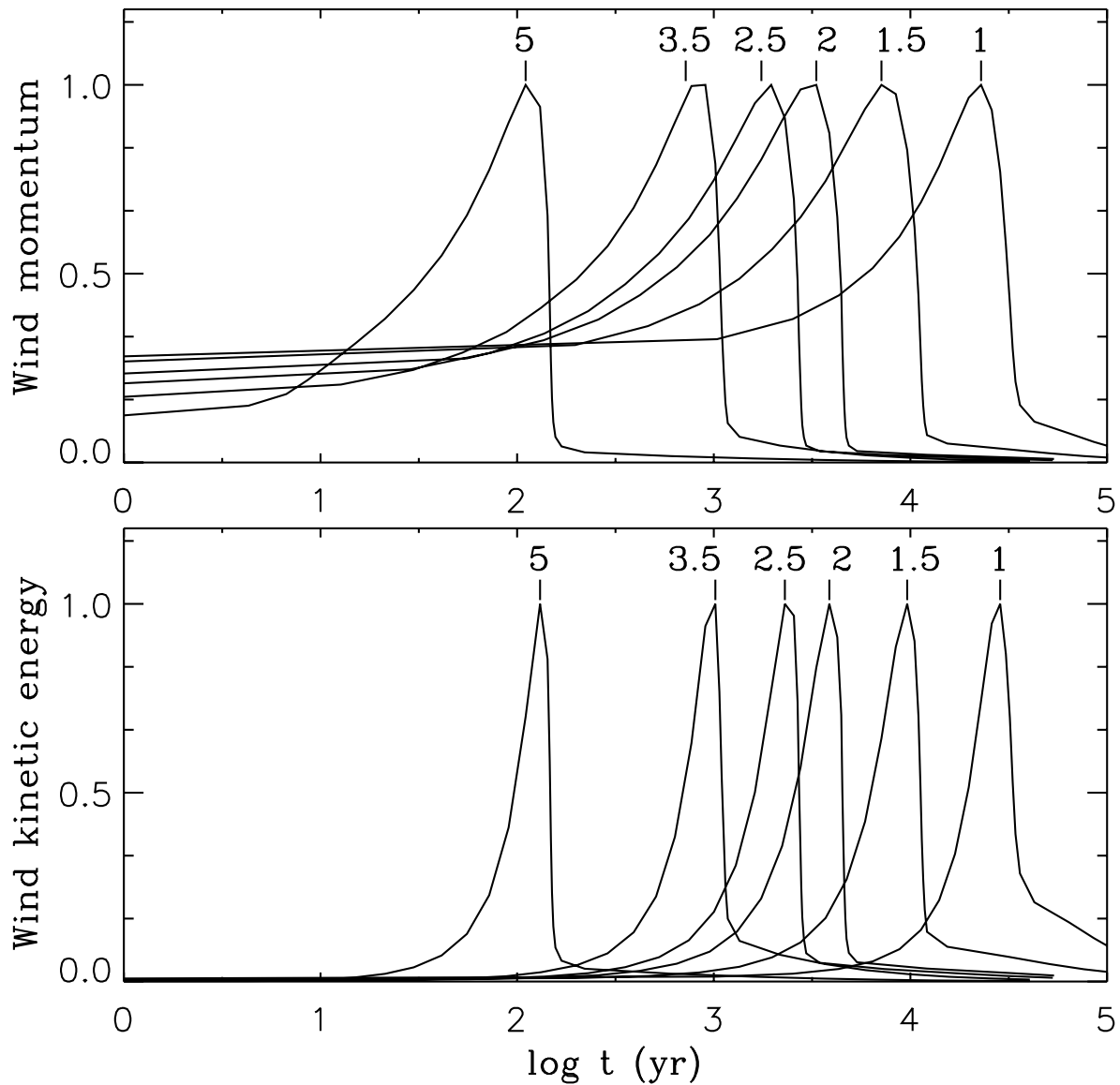


Fig. 3.— Upper panel: wind momentum versus time on a logarithmic scale. Each curve has been normalized to its maximum value and marked with the initial mass of the star. Lower panel: the same for the wind kinetic energy.

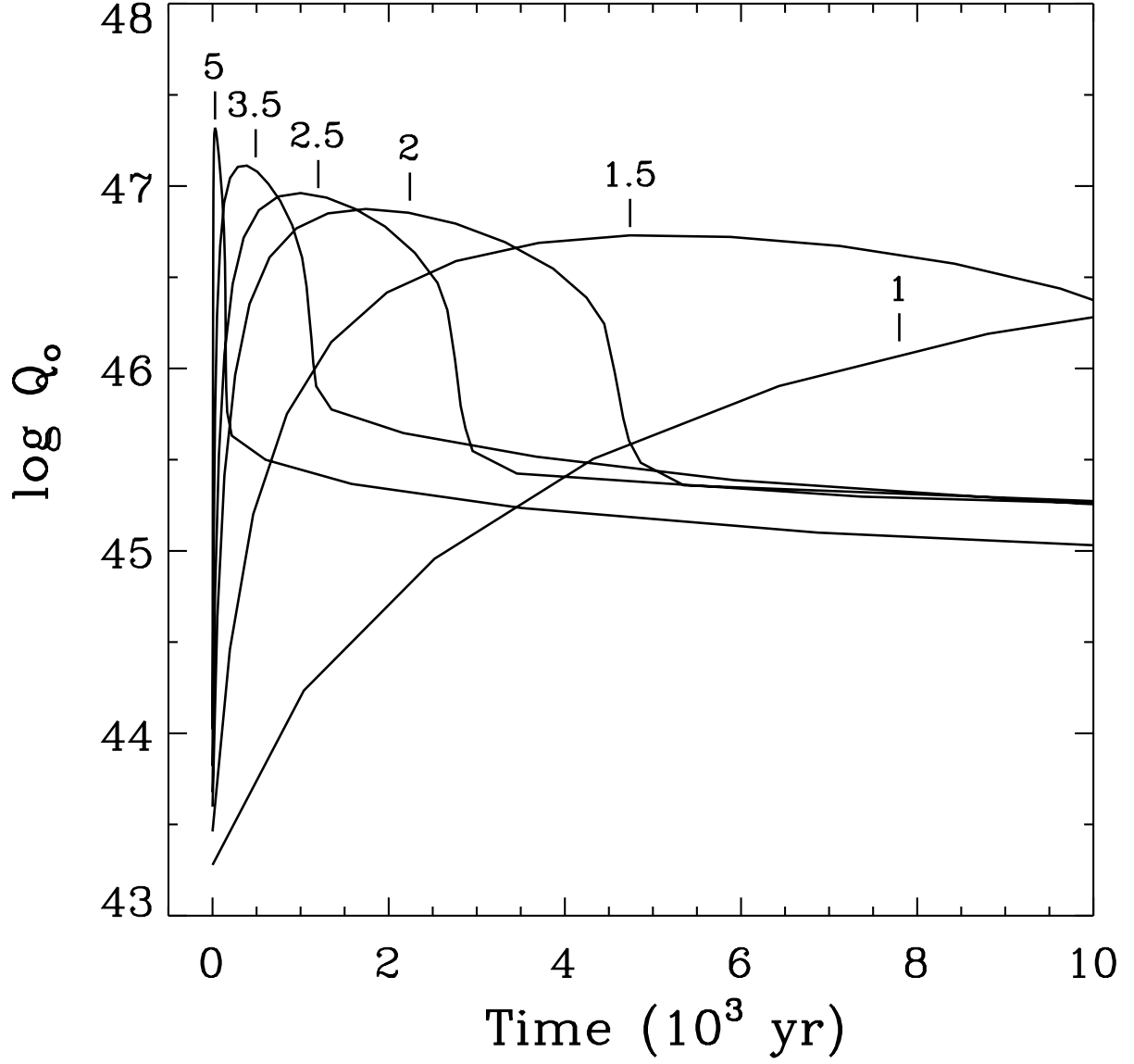


Fig. 4.— Number of ionizing photons,  $Q_0$  (on a logarithmic scale), during the first 10 000 yr of CS evolution. Each line has been marked with the initial mass of the model.

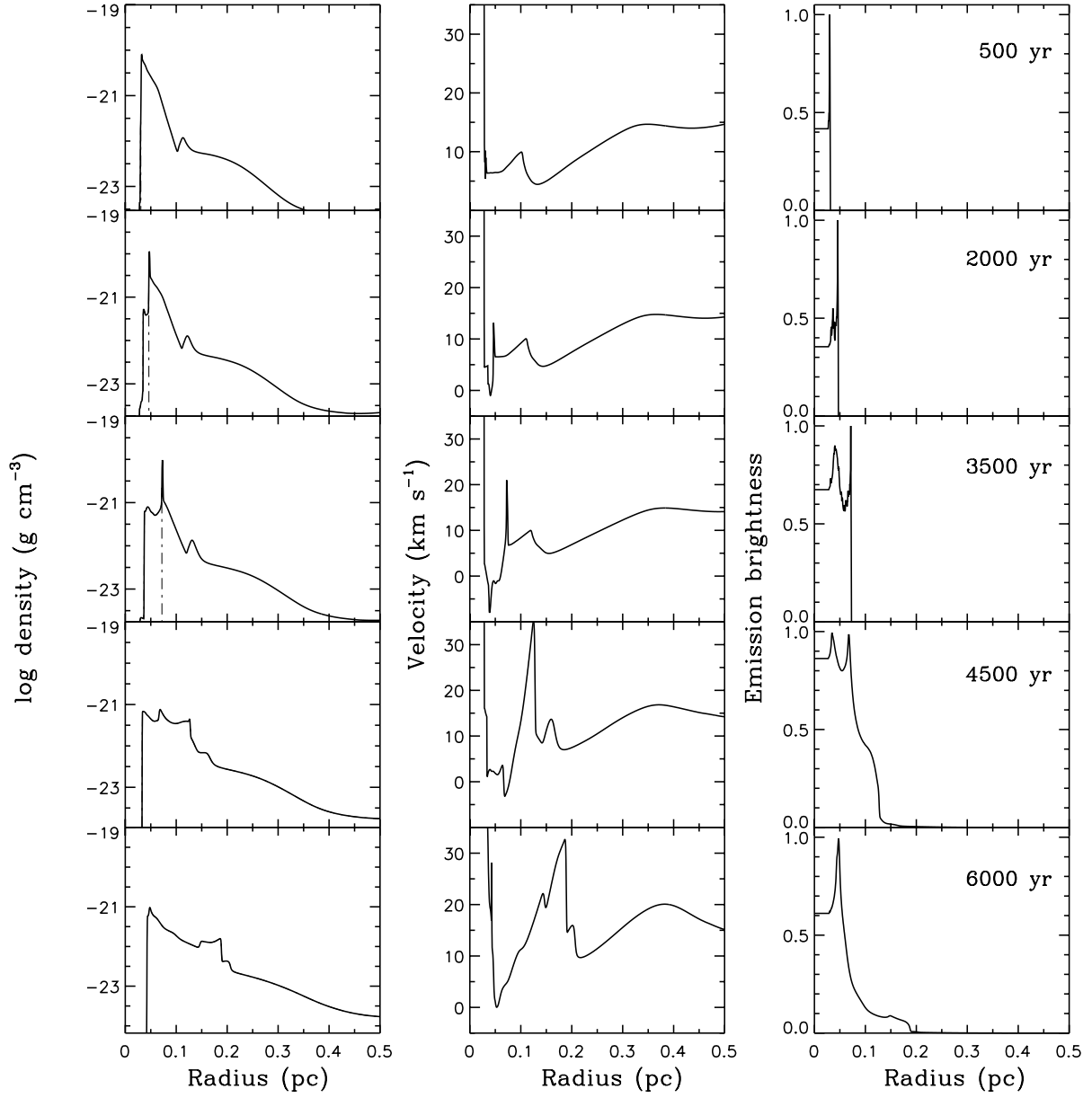


Fig. 5.— Density, velocity, and H $\alpha$  EBP radial distributions at different evolutionary times during the PN stage for the  $1 M_{\odot}$  stellar model. The position of the IF is marked as a dotted line in the density profile.

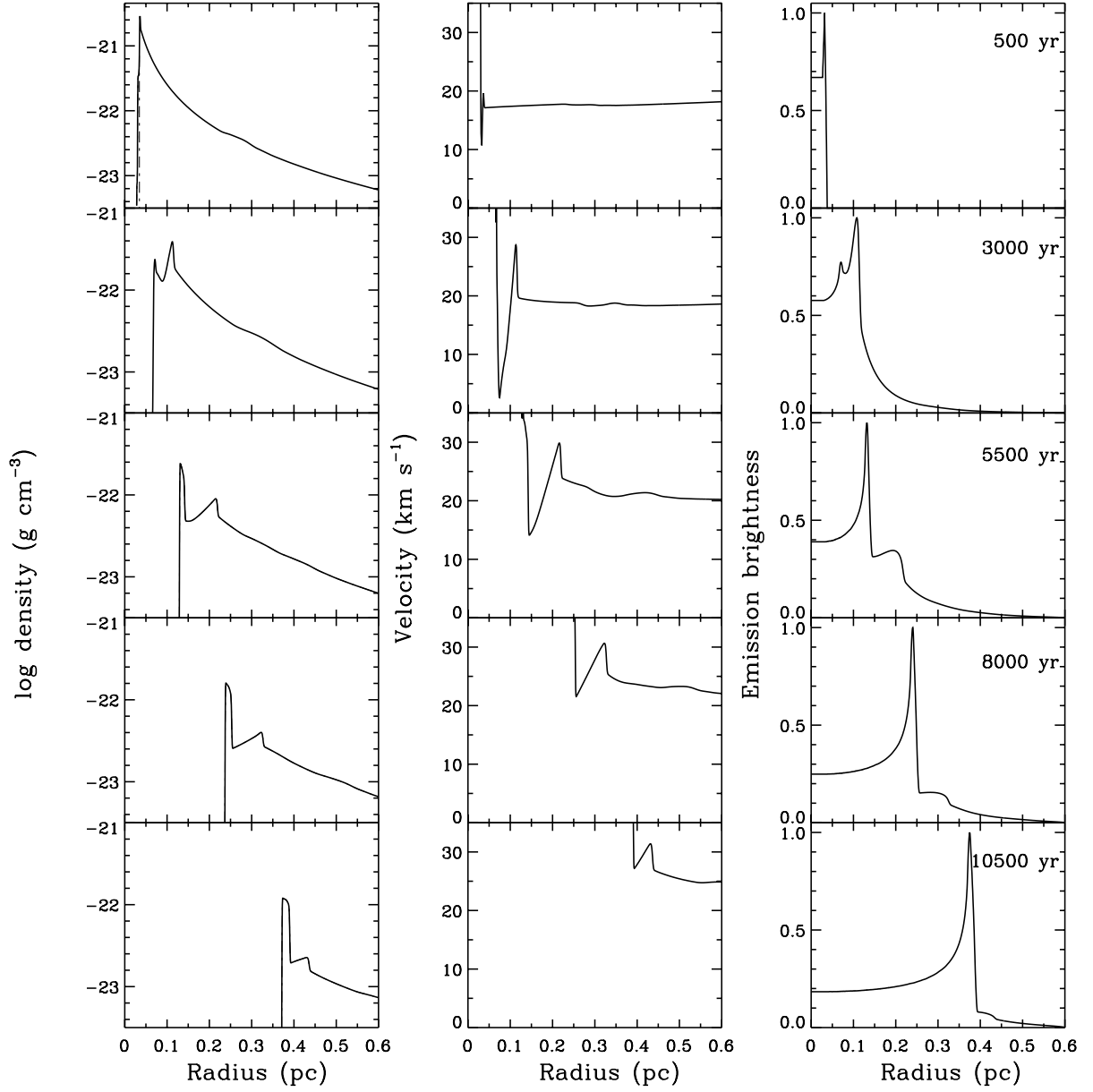


Fig. 6.— Same as Figure 5, but for the  $1.5 M_{\odot}$  stellar case.



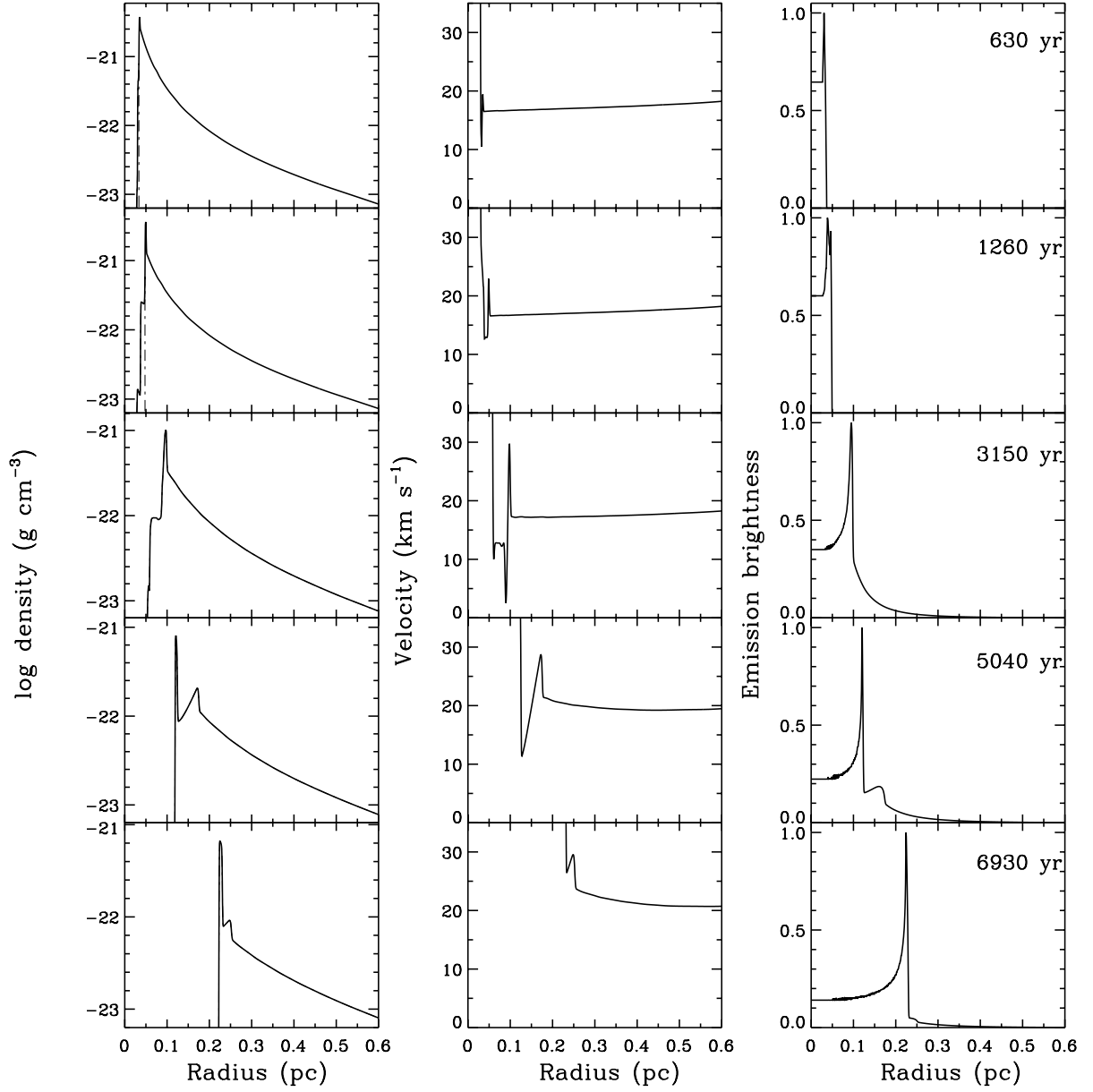


Fig. 7.— Same as Figure 5, but for the  $2 M_{\odot}$  stellar case.

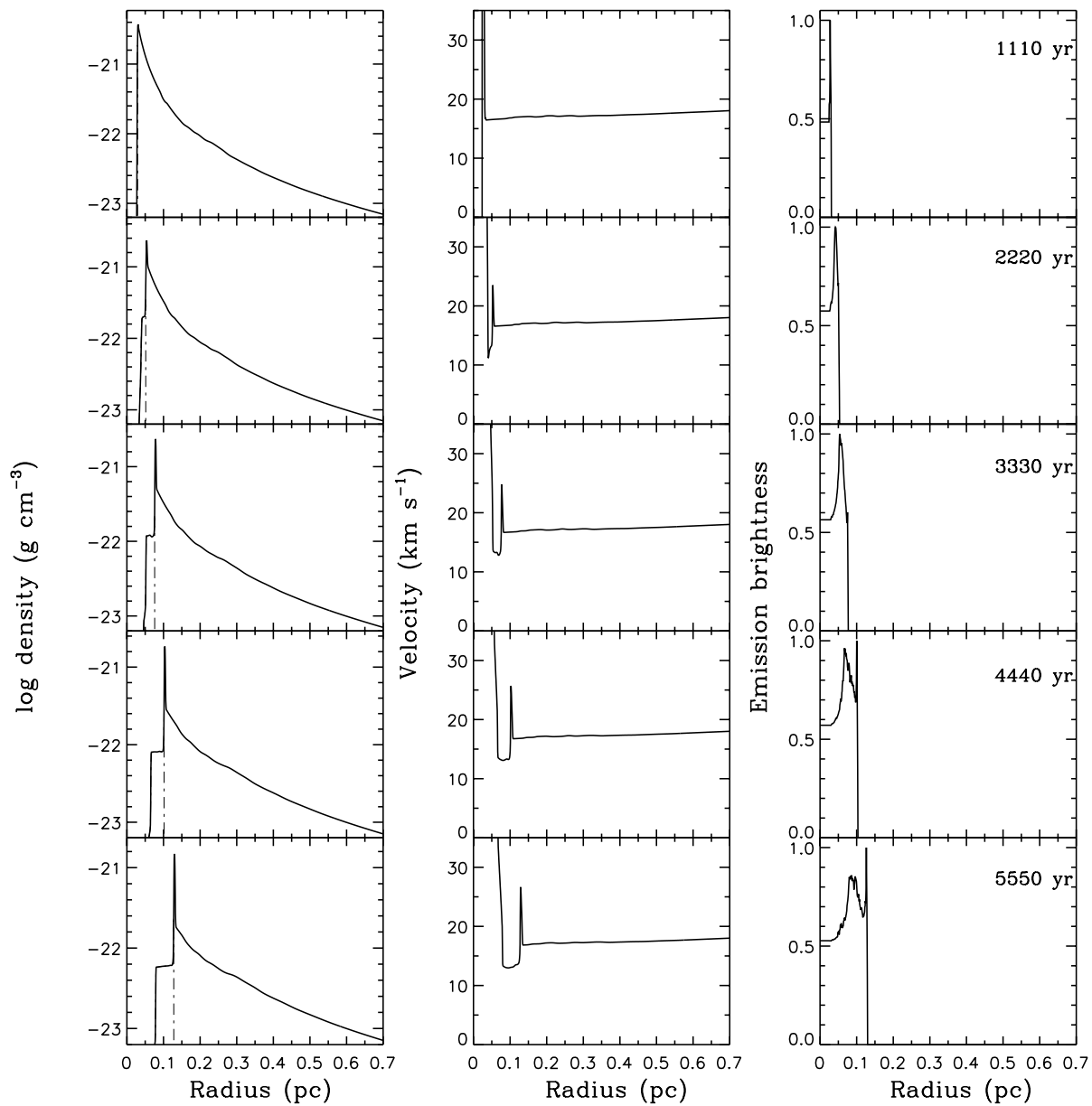


Fig. 8.— Same as Figure 5, but for the  $2.5 M_{\odot}$  stellar case.

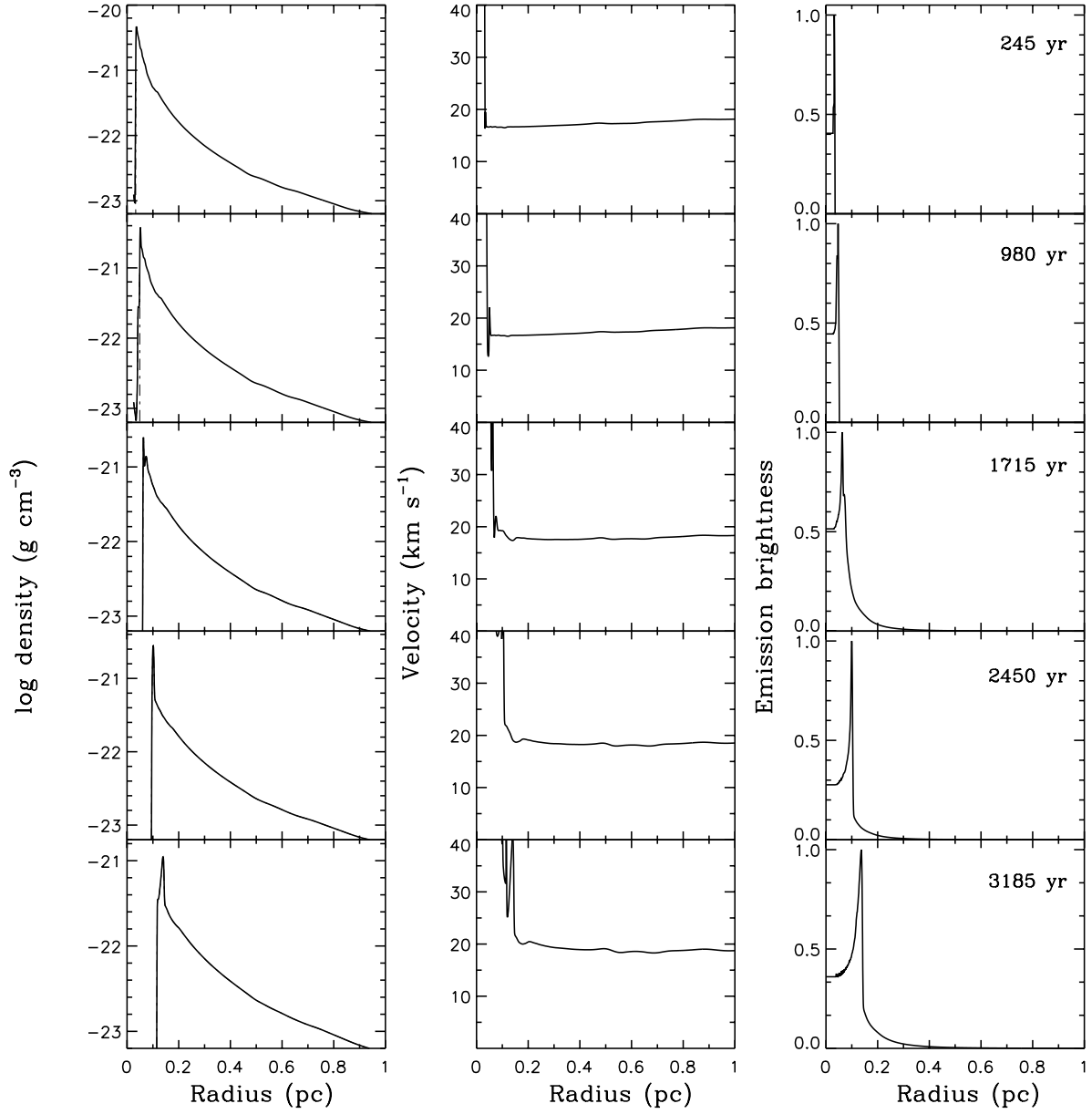


Fig. 9.— Same as Figure 5, but for the  $3.5 M_{\odot}$  stellar case.

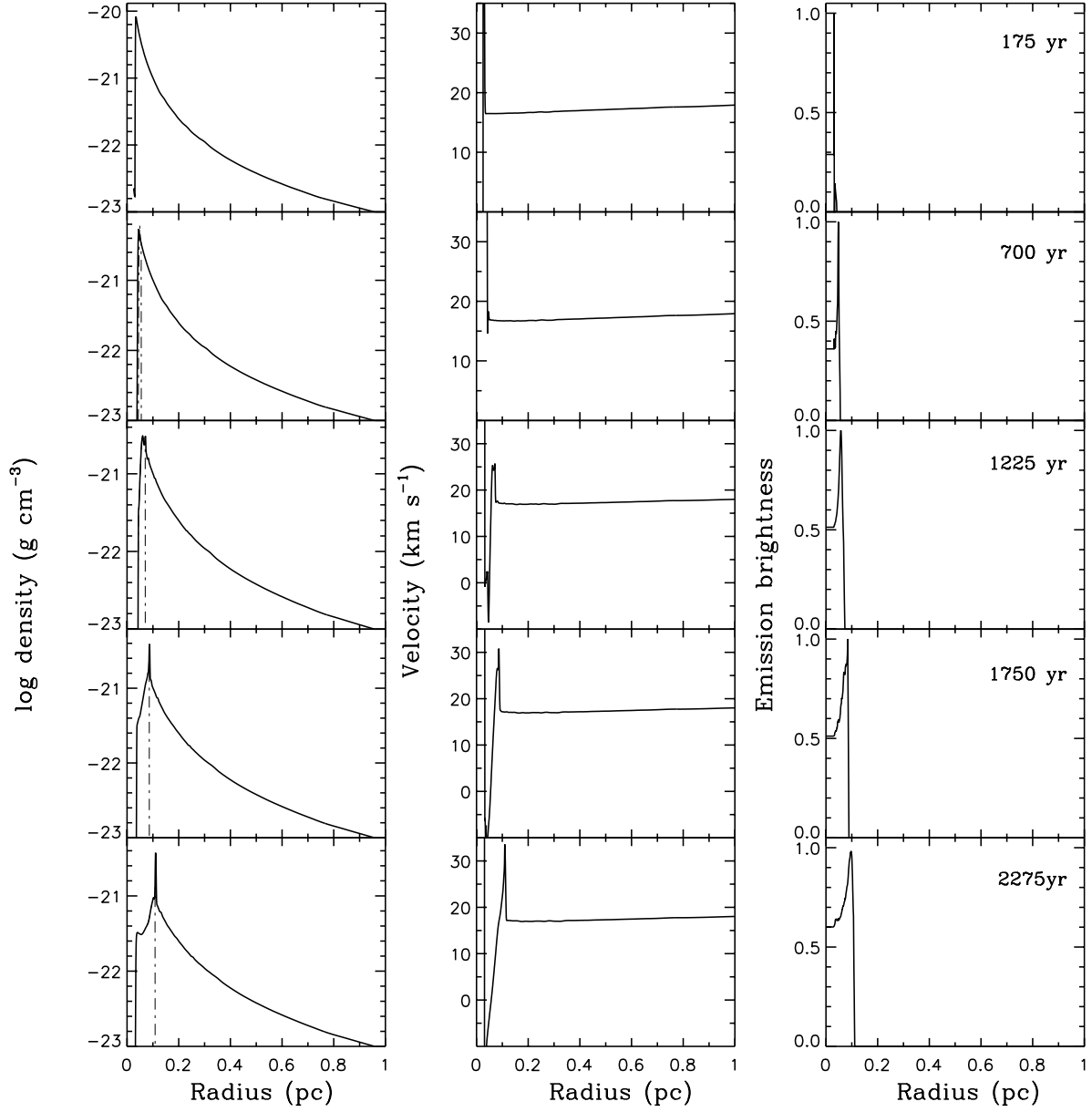


Fig. 10.— Same as Figure 5, but for the  $5 M_{\odot}$  stellar case.

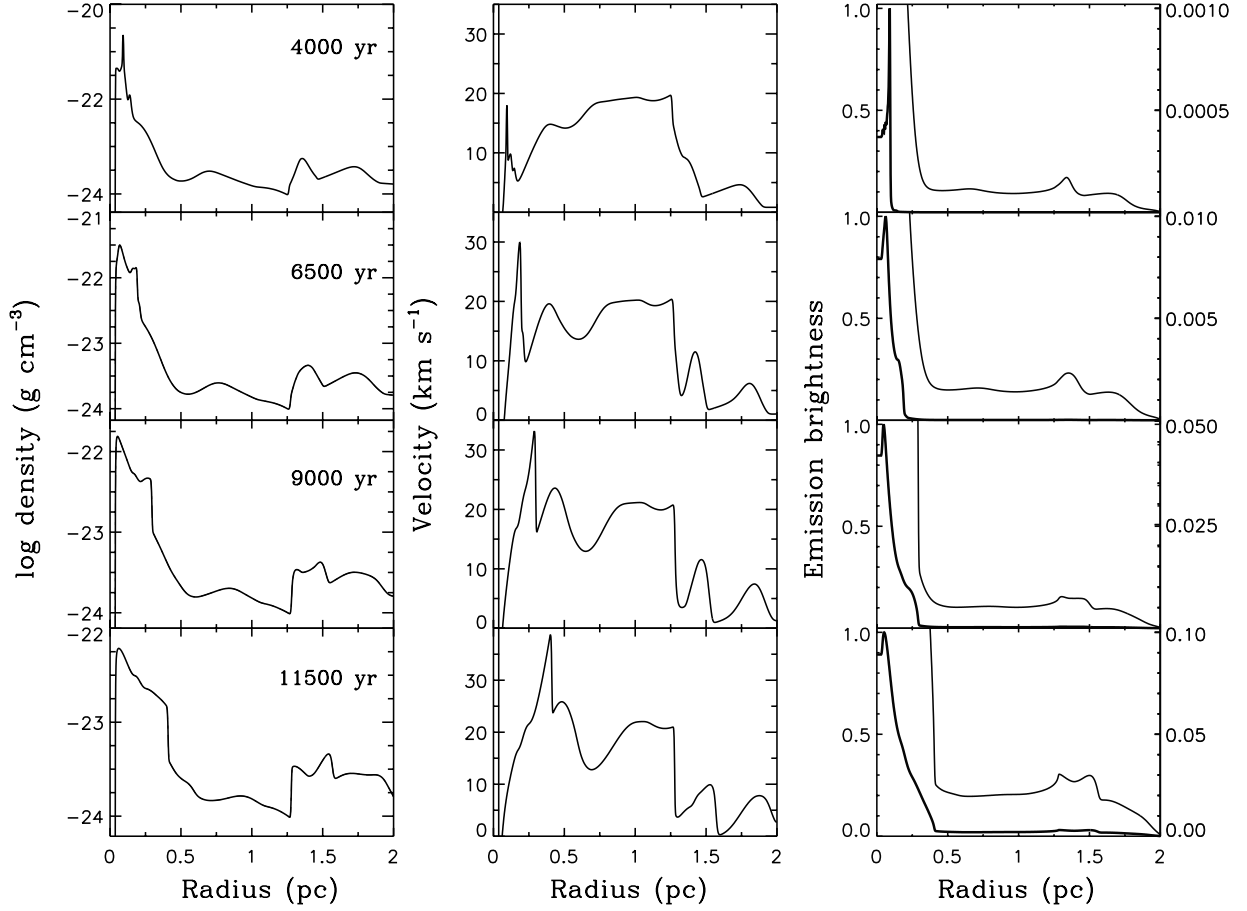


Fig. 11.— Density, velocity, and EBP radial distributions of the large-scale structure of the gas for the  $1 M_{\odot}$  stellar case. The EBP are shown on two scales: the scale on the left is for the EBP of the bright main nebula, which is shown with a thick line; the scale on the right corresponds to the thin line, which shows the EBP of the much fainter outer regions of the nebula.

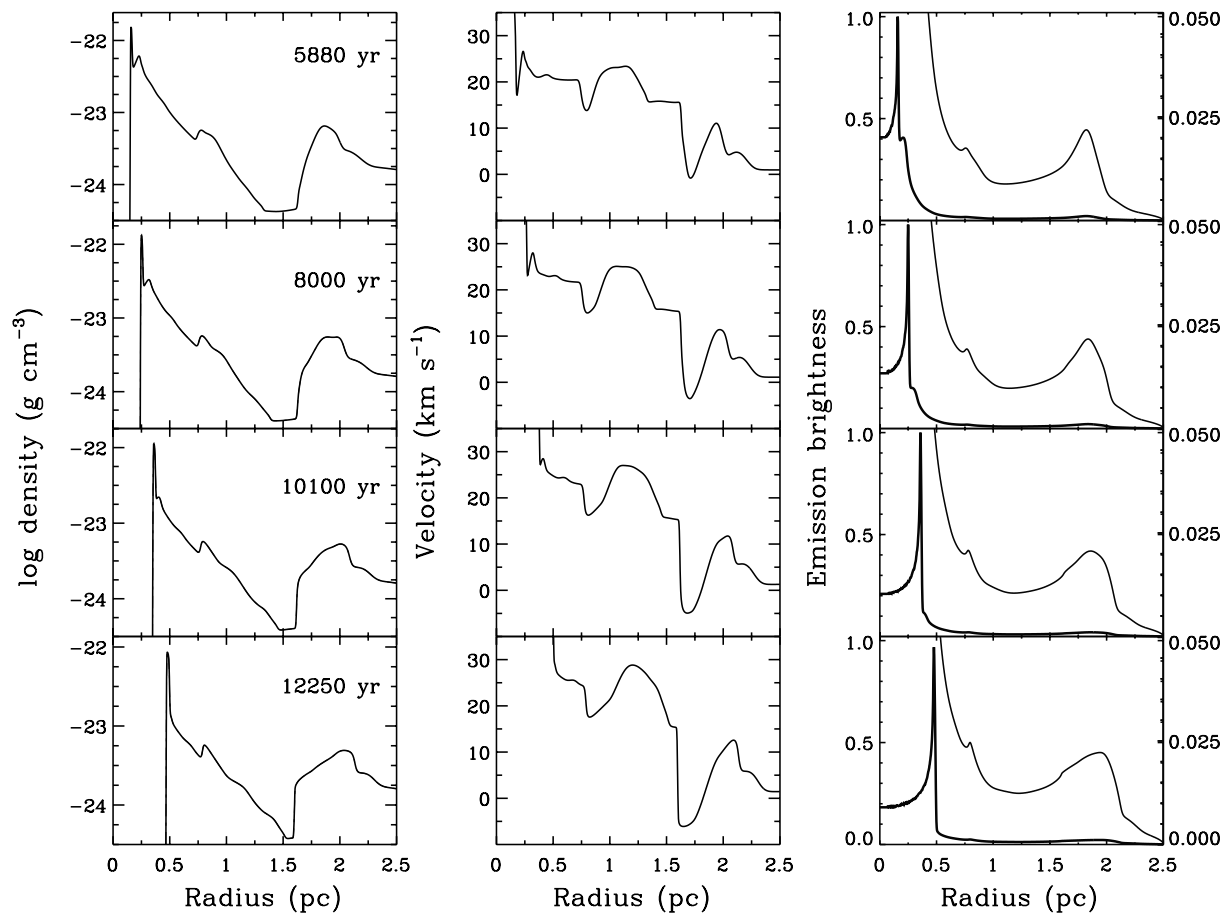


Fig. 12.— Same as Figure 11, but for the  $1.5 M_{\odot}$  stellar case.

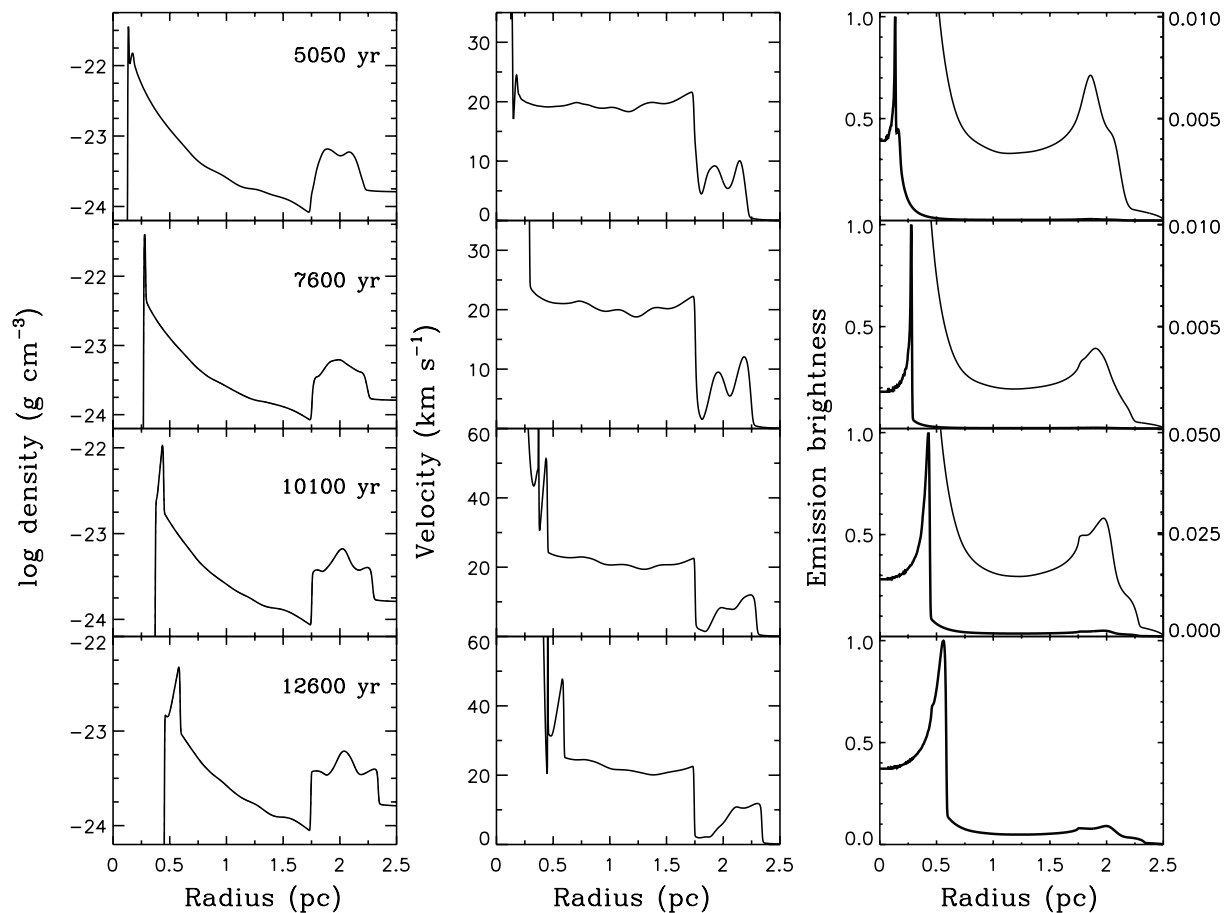


Fig. 13.— Same as Figure 11, but for the  $2 M_{\odot}$  stellar model.

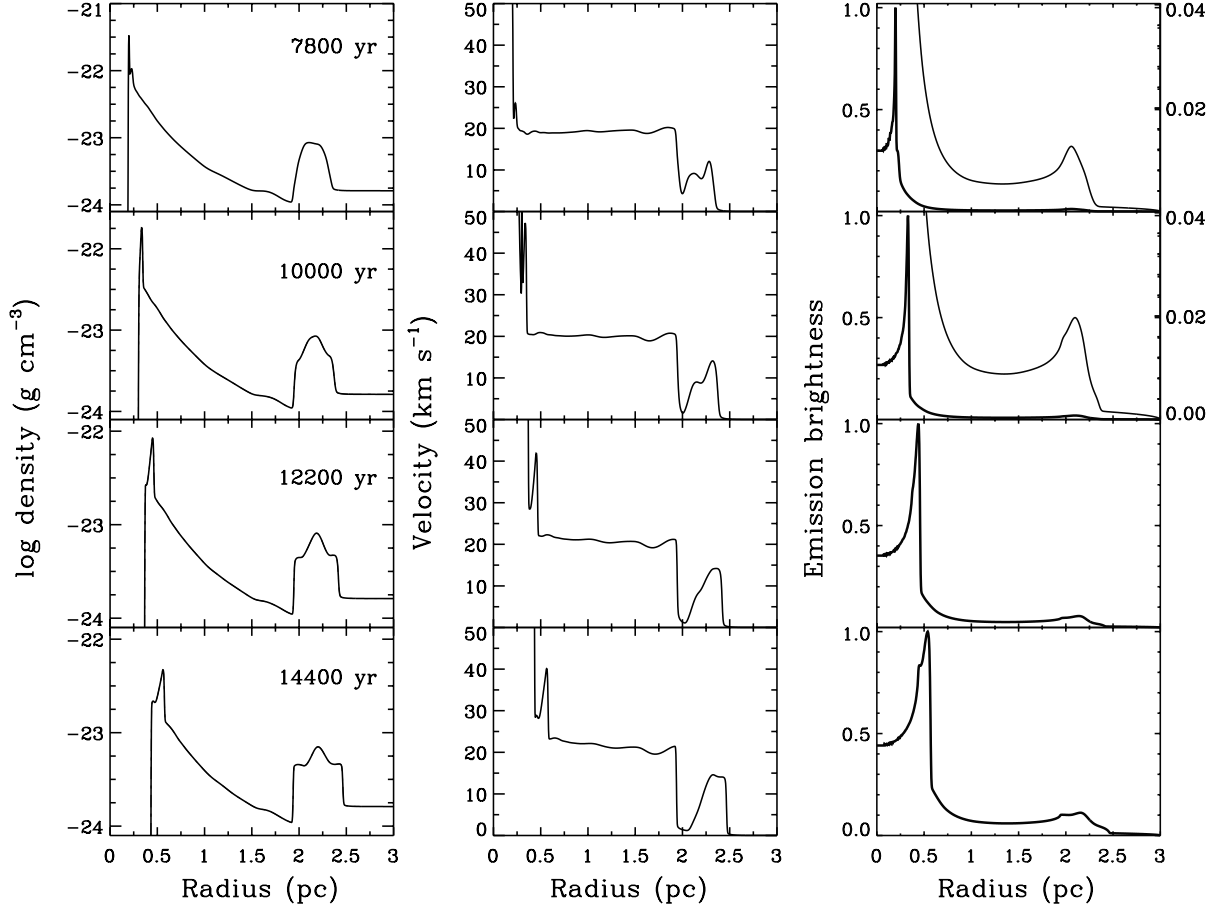


Fig. 14.— Same as Figure 11, but for the  $2.5 M_{\odot}$  stellar model.



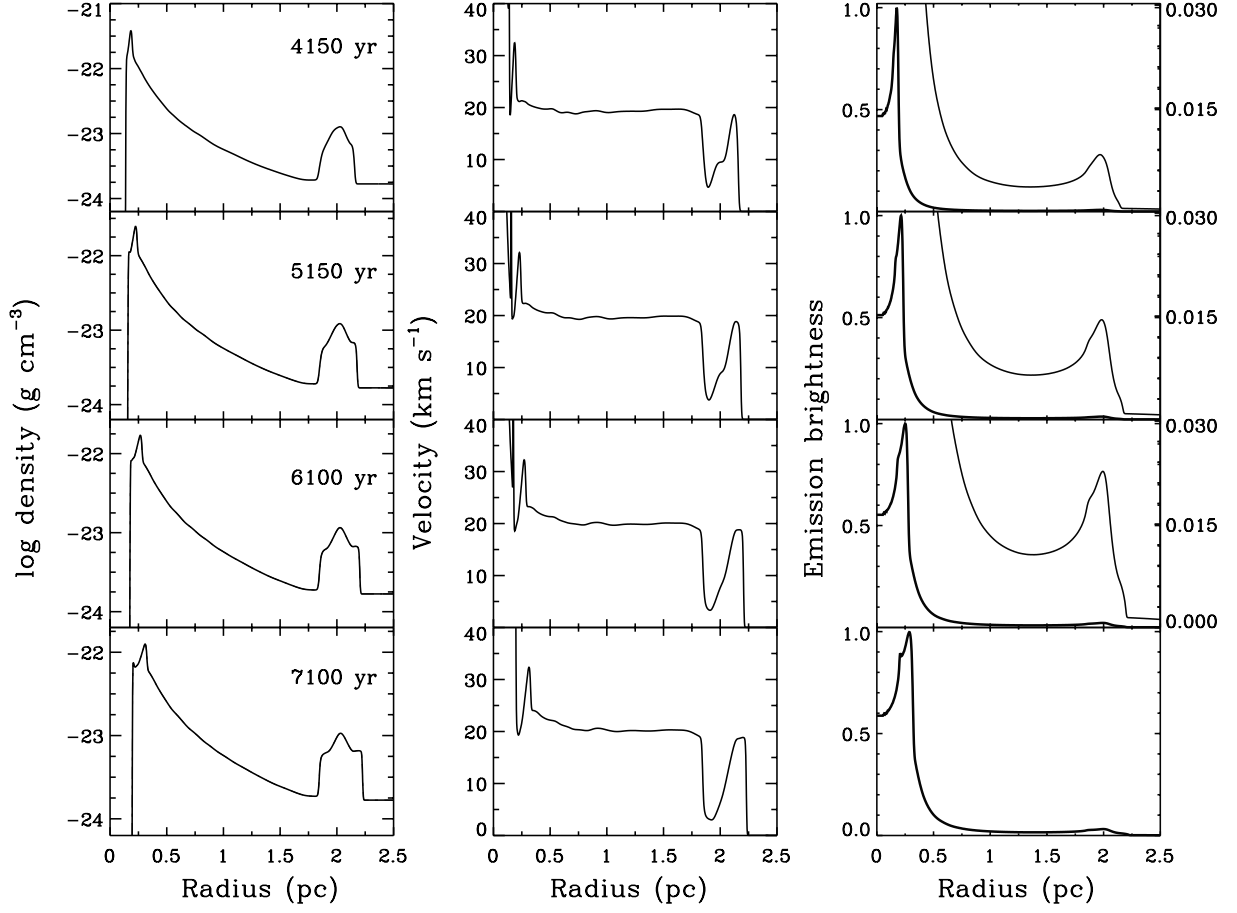


Fig. 15.— Same as Figure 11, but for the  $3.5 M_{\odot}$  stellar model.

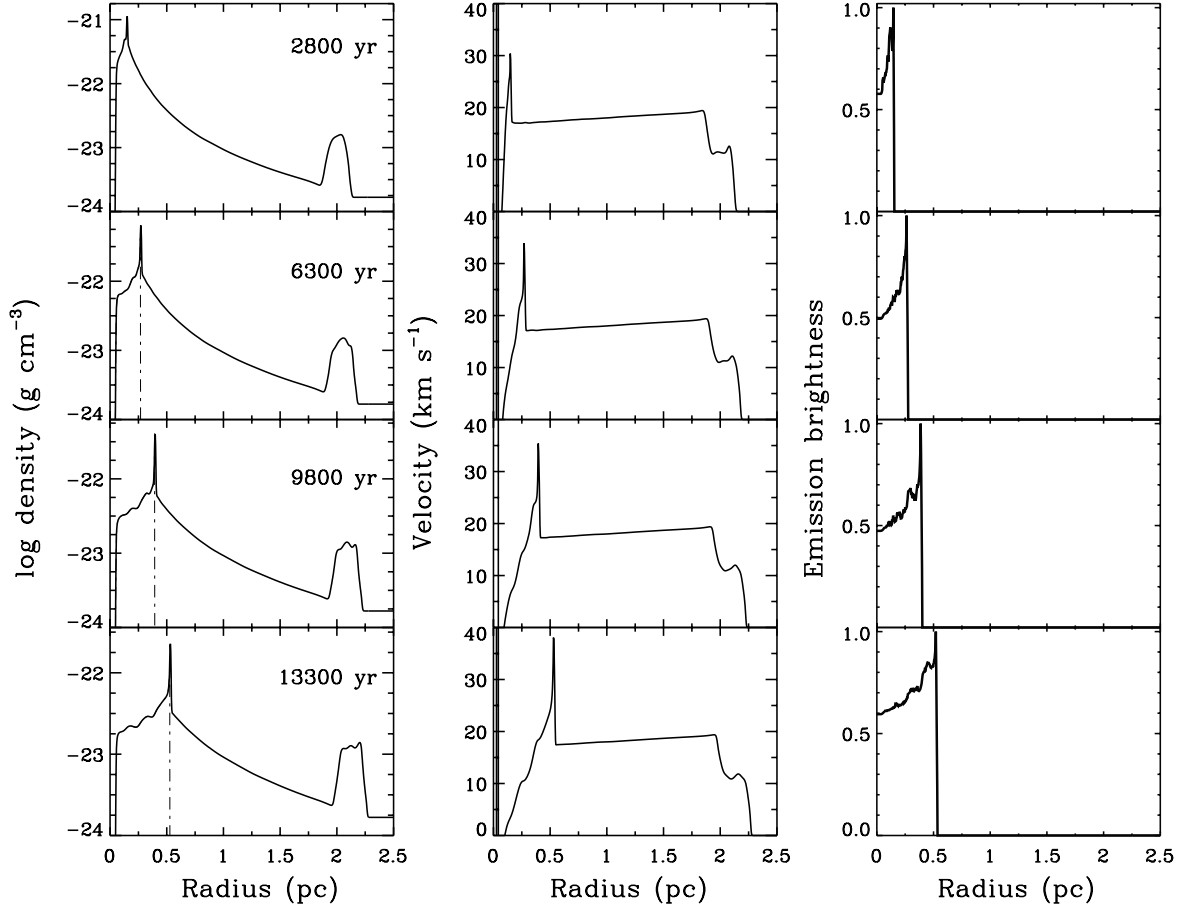


Fig. 16.— Same as Figure 11, but for the  $5 M_{\odot}$  stellar model.

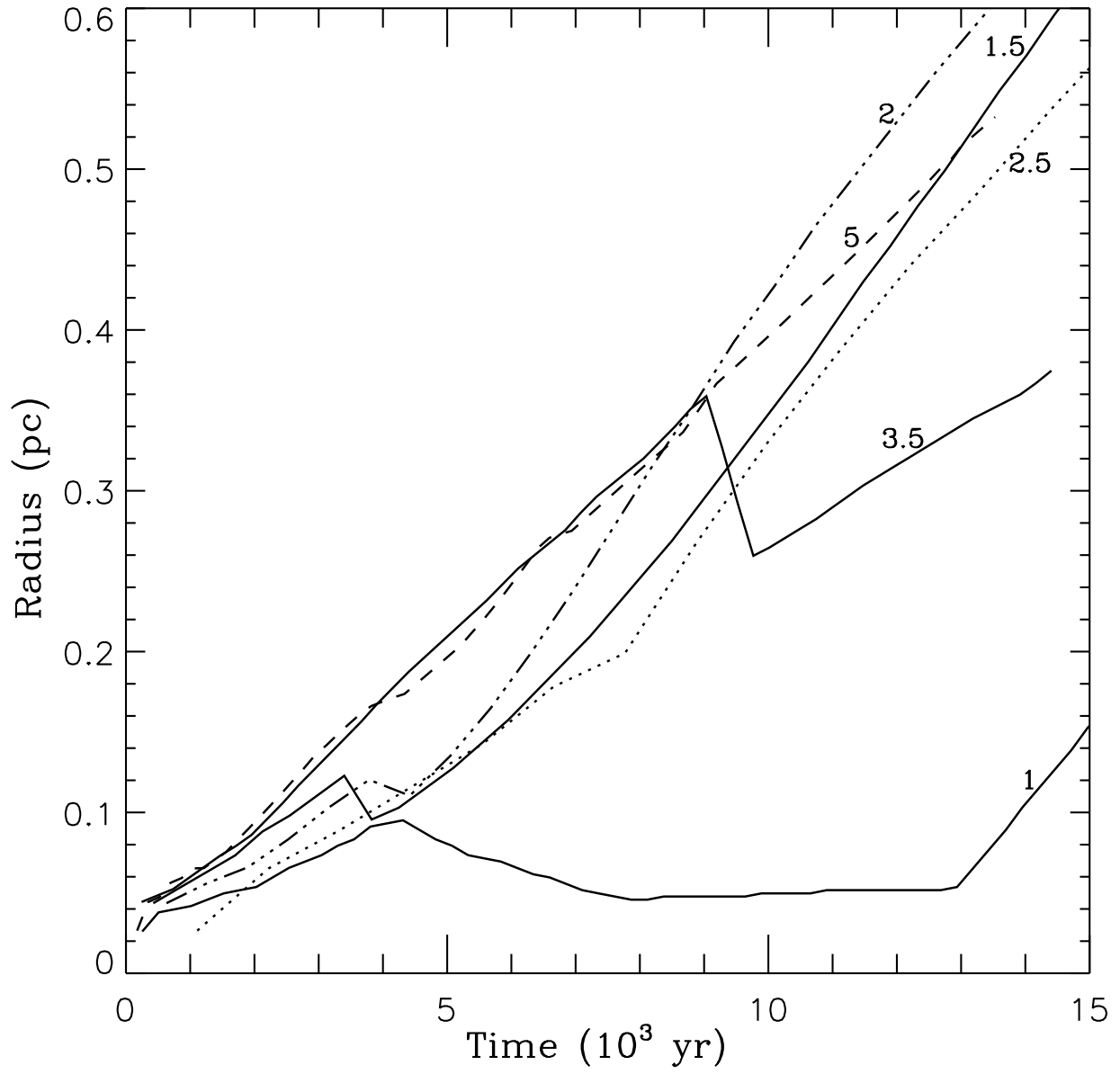


Fig. 17.— Evolution of the radius of the main shell. The initial mass of the model is marked on each line.

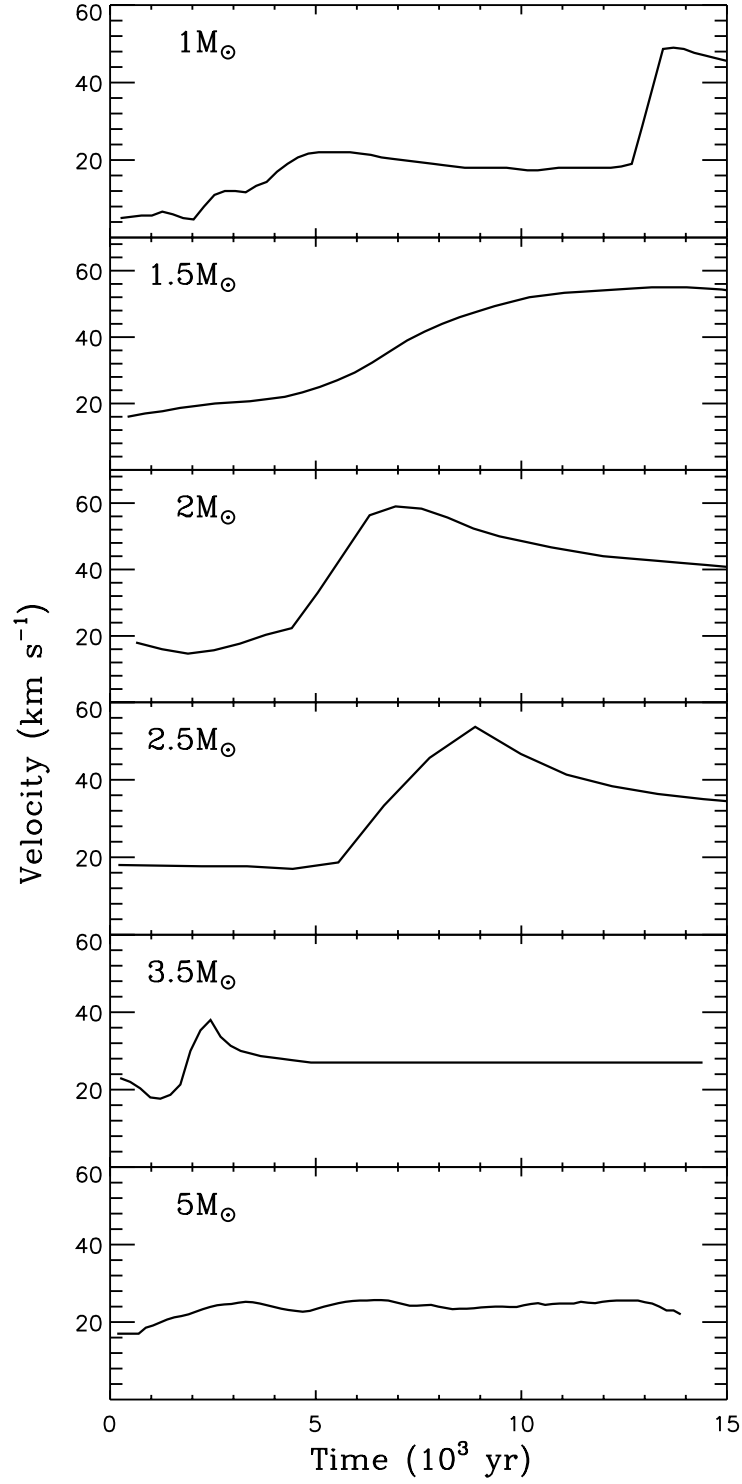


Fig. 18.— Temporal evolution of the velocity of the main shell. From top to bottom, we show the 1, 1.5, 2, 2.5, 3.5 and 5  $M_{\odot}$  models. The velocities have been computed by fitting Gaussians to the synthetic spectra across the center of the nebula.

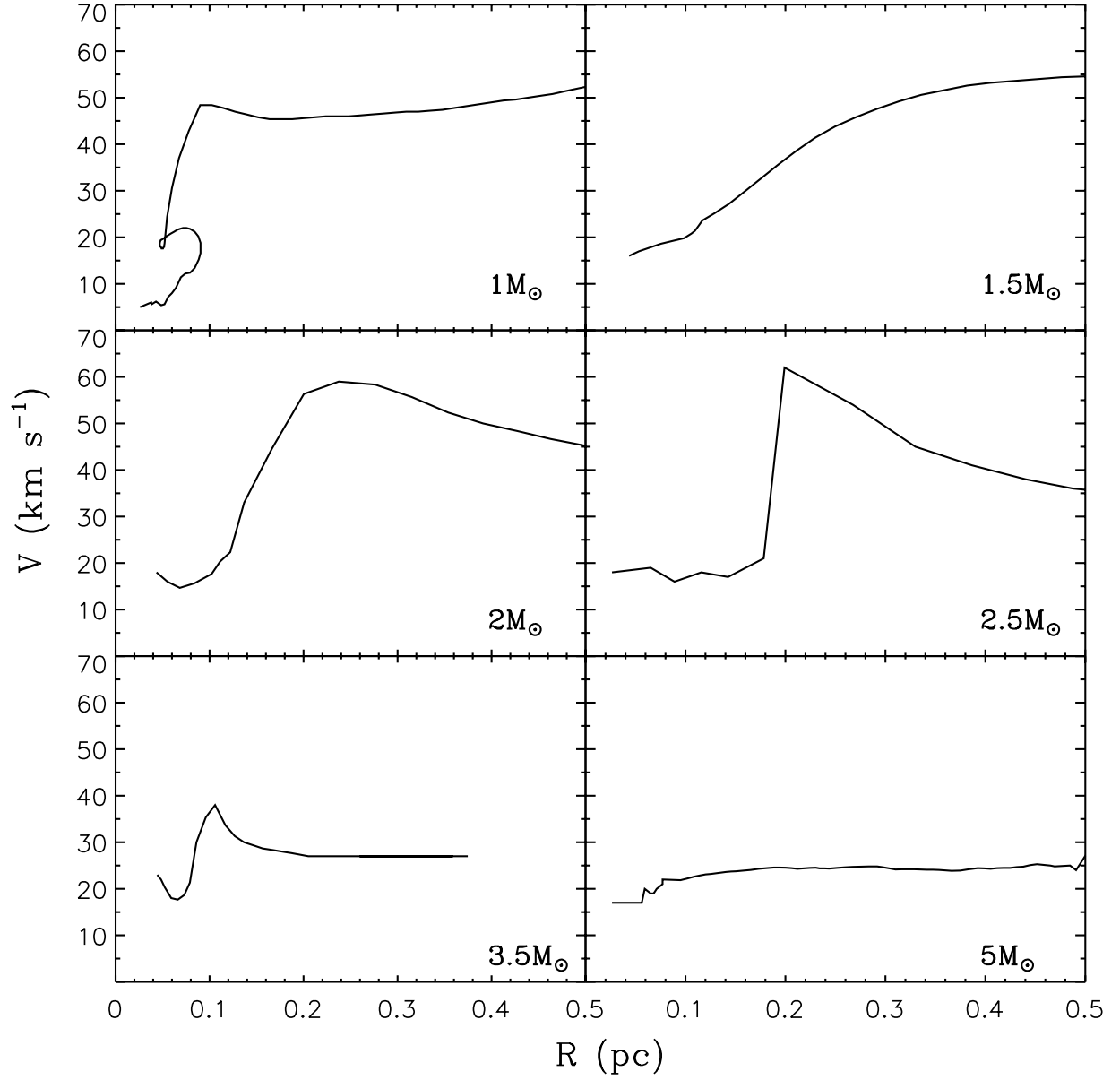


Fig. 19.— Expansion velocity versus radius for the main shells. From top to bottom and from left to right, we show the 1, 1.5, 2, 2.5, 3.5, and 5  $M_{\odot}$  models.

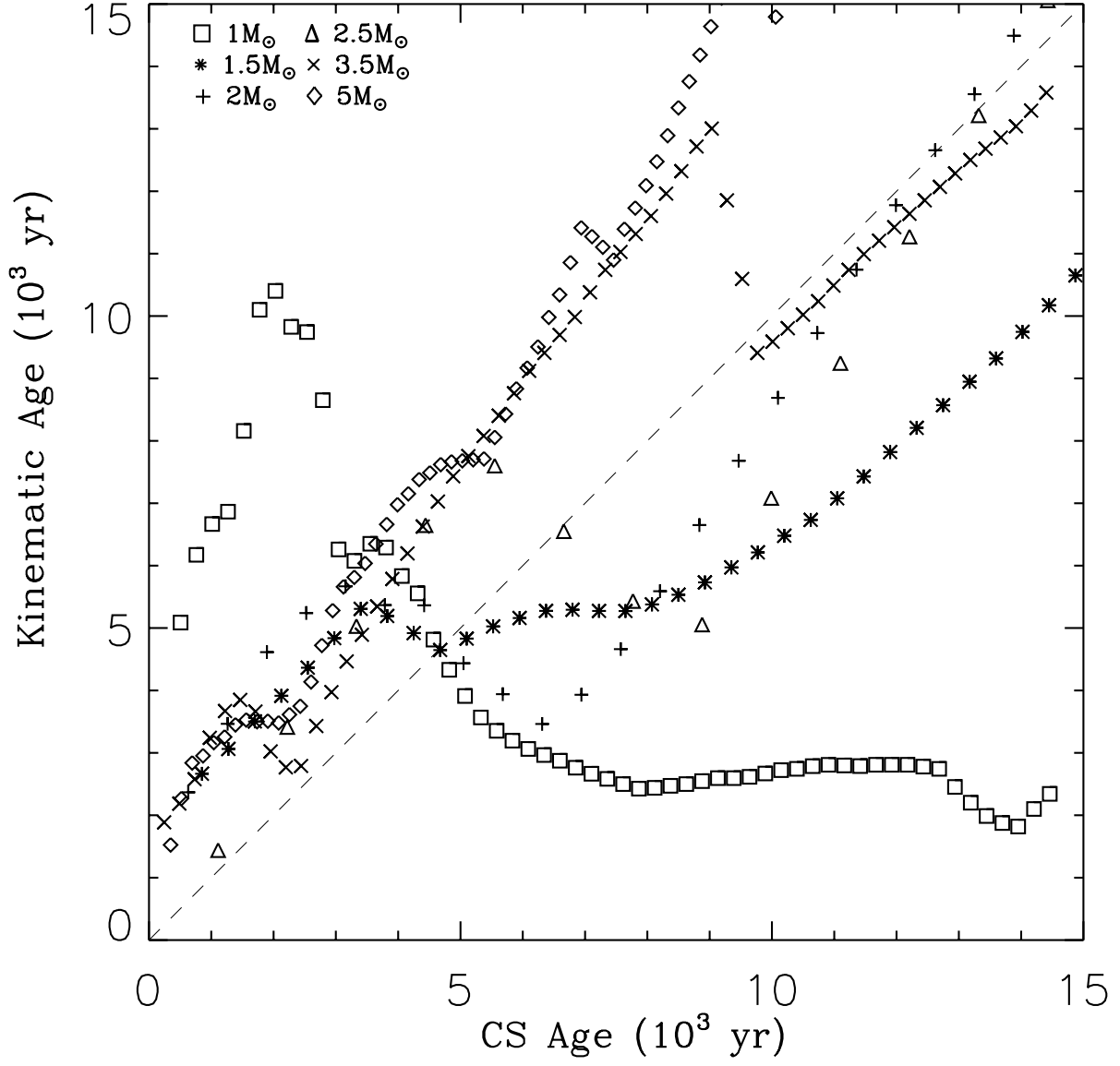


Fig. 20.— Kinematical ages derived from our simulations using standard procedures are plotted versus the CS ages. The symbols used for the different models are shown in the top left corner of the plot.

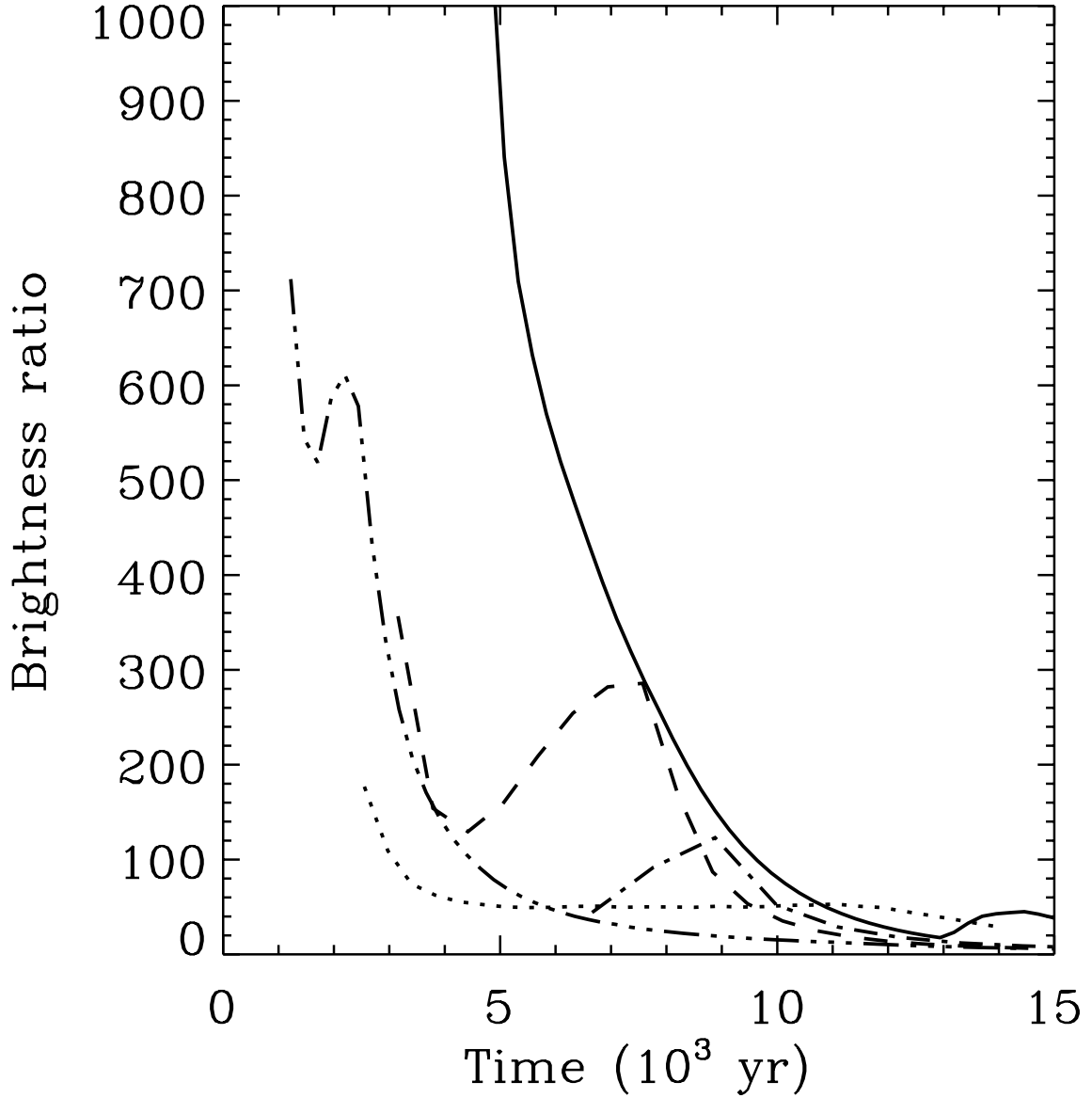


Fig. 21.— Evolution of the  $H\alpha$  peak emissivity ratio of the inner region with respect to that of the detached halos. The solid line represents the values for the  $1 M_\odot$  case, while the dotted, dashed, dash-dotted, and dash-dot-dot-dotted lines represent the ratio for the 1, 1.5, 2, 2.5, and  $3.5 M_\odot$  models respectively.

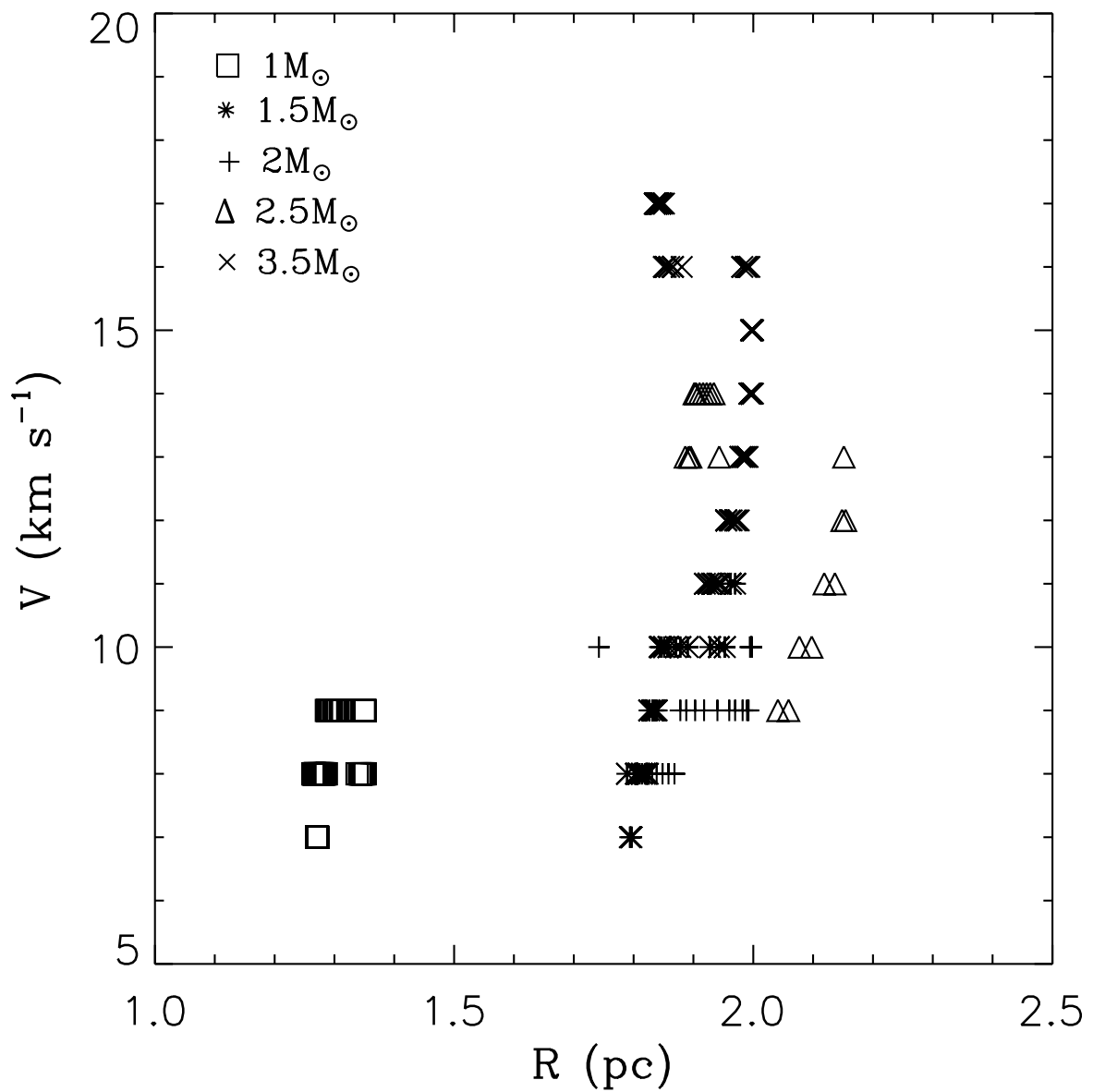


Fig. 22.— Velocity of the outer detached shell plotted versus its radius. The temporal evolution of the detached shell has been followed up to  $10^5$  yr and the points represent the values measured for each output of the simulations.



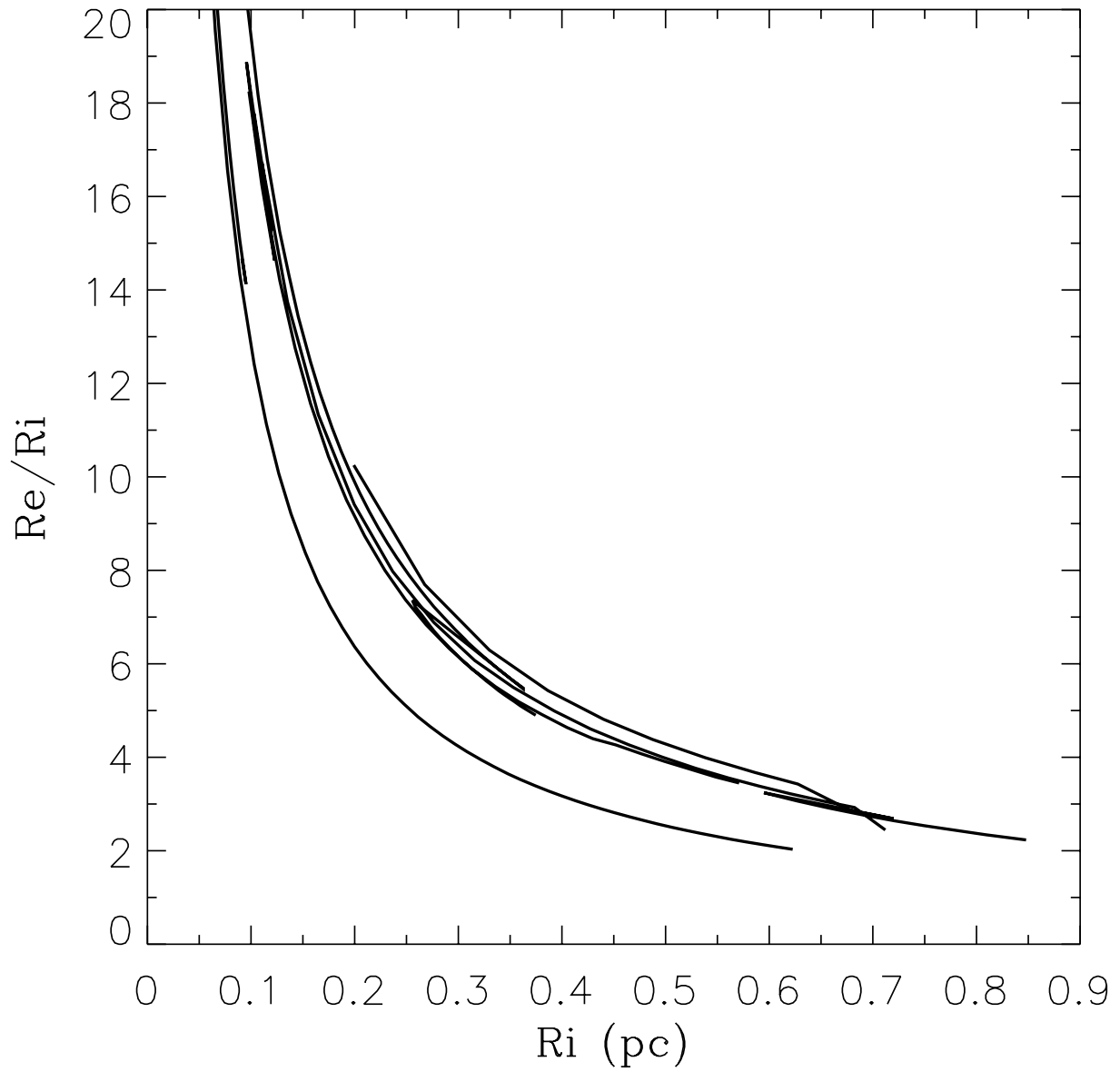


Fig. 23.— Ratio of the outer detached shell to main shell radii plotted versus the radius of the main shell. The values shown go from the onset of the ionization of the outer shell up to  $10^5$  yr.

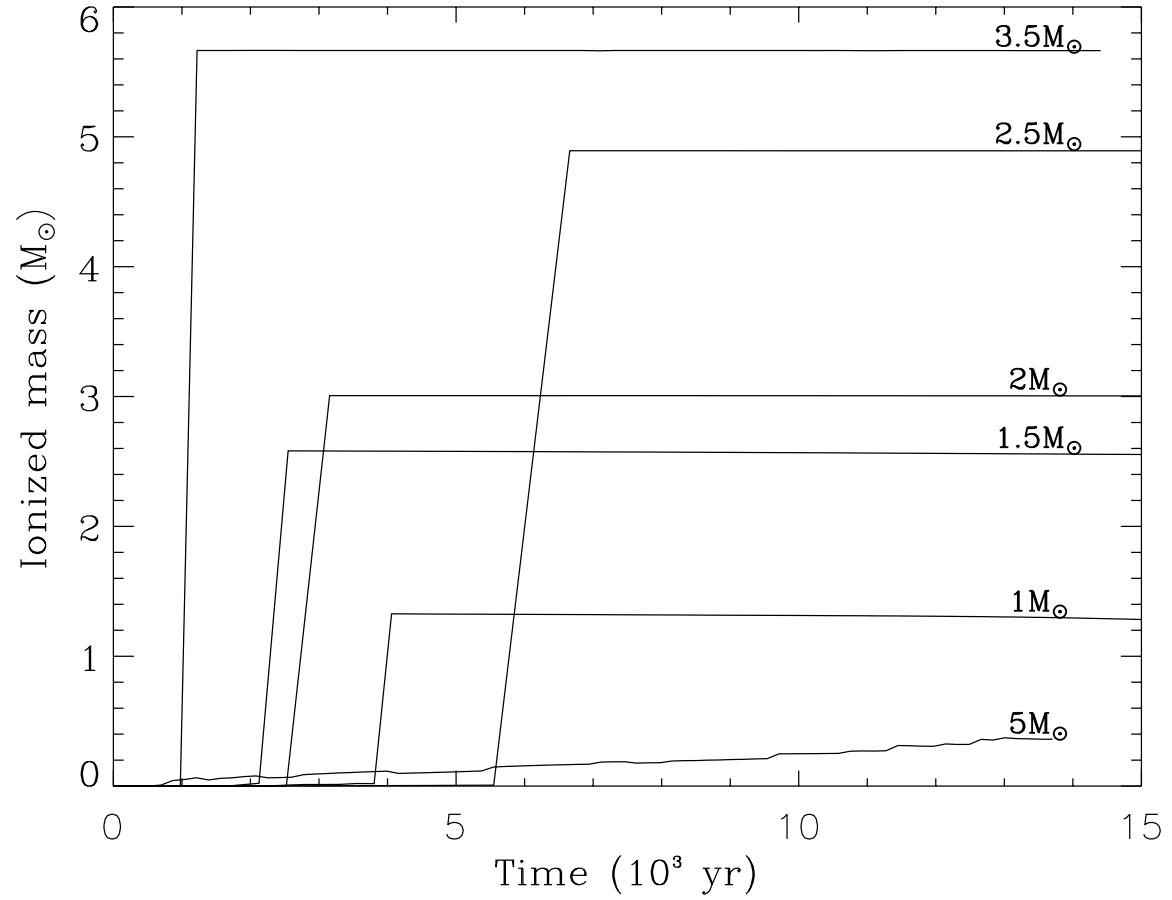


Fig. 24.— Ionized mass in the grid versus time. The initial mass of the model is indicated in each curve.

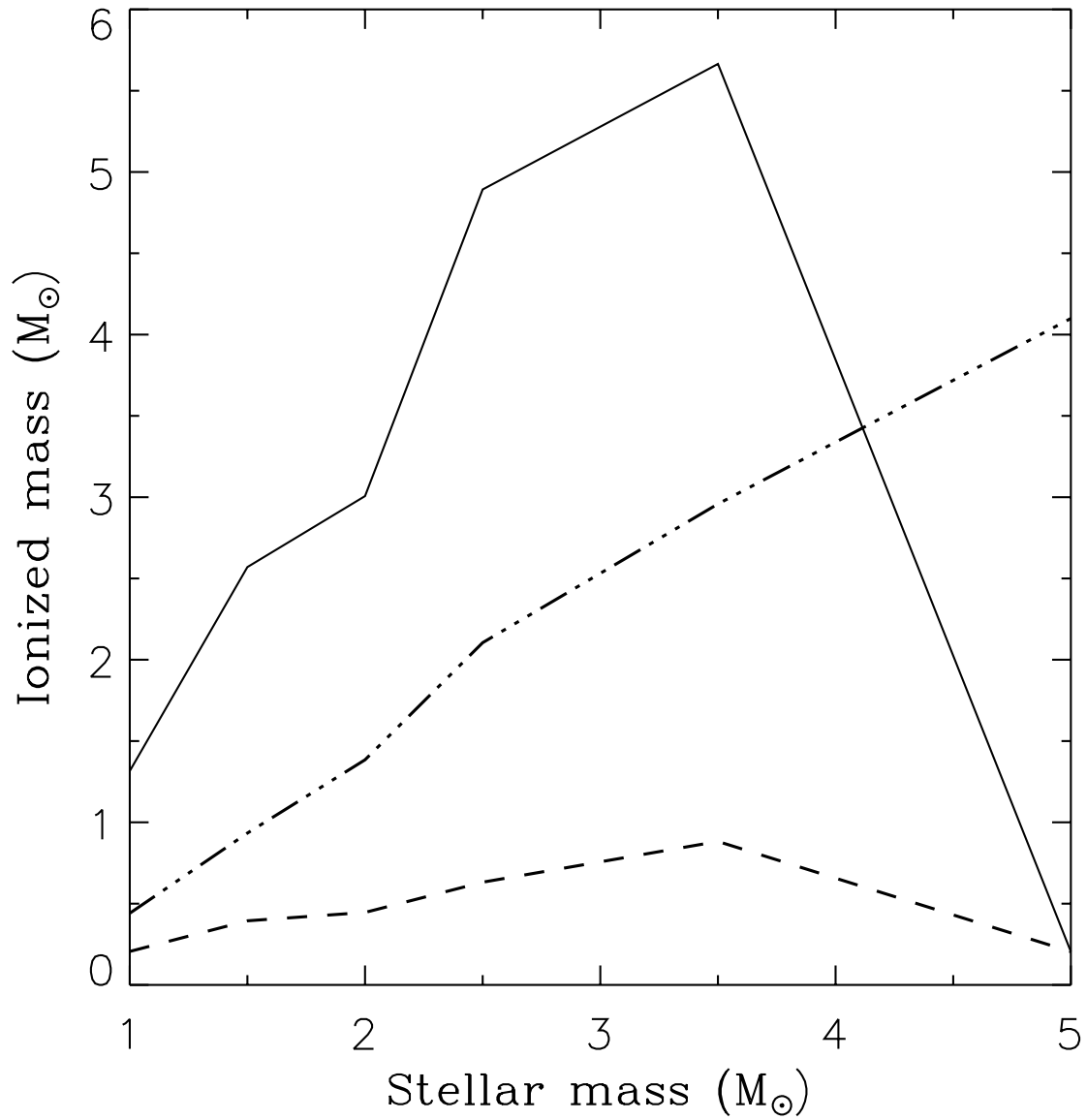


Fig. 25.— Ionized mass (solid line), total mass lost by the star (dot-dashed line), and ionized mass contained in the main shell (dashed line) for the different initial masses considered in the models.